Direct pharmacological AMPK activation inhibits mucosal SARS-CoV-2 infection by reducing lipid metabolism, restoring autophagy flux and the type I IFN response

Andrea Cottignies-Calamarte[1,2], Flora Marteau[1,2], Feifan He[1,2], Sandrine Belouzard[3], Jean Dubuisson[3], Daniela Tudor[1,2], Benoit Viollet[2] and Morgane Bomsel[1,2,#]

[1]Laboratory of Mucosal Entry of HIV and Mucosal Immunity Institut Cochin, Paris France

[2]Université Paris Cité, CNRS, Inserm, Institut Cochin, Paris, France,

[3]Virologie moléculaire et cellulaire des coronavirus, Centre d'infection et d'immunité de Lille, Institut Pasteur de Lille, Université de Lille, CNRS, Inserm, CHRU, 59000 Lille, France

#: Corresponding author: morgane.bomsel@inserm.fr

Graphical abstract

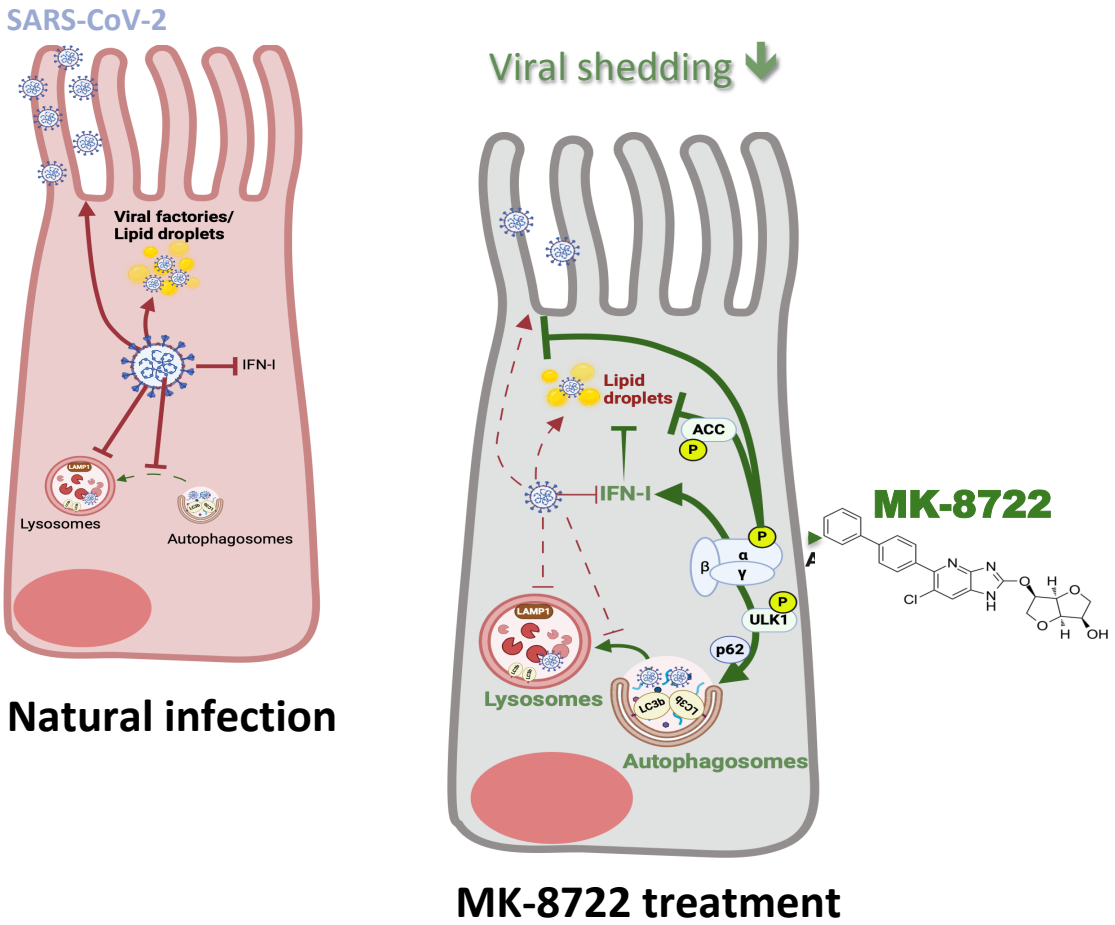

Highlights

- **MK-8722 exerts post-exposure antiviral activity**
- **MK-8722 induces a decrease in cellular lipid content**
- **MK-8722 promotes an increase in the autophagic flux of viral components**
- **MK-8722 promotes the restoration of the IFN-I activity**
- **MK-8722 antiviral activity is compatible with virus-specific T cell responses**

Abstract

AMP-activated protein kinase (AMPK) plays a central role in regulating cell energy balance. When activated, AMPK supresses energy-consuming pathways such as lipid and protein synthesis while increasing nutrient availability through the activation of autophagy. These pathways downstream AMPK activation contribute to SARS-CoV-2 infection, which hijacks autophagy and accumulates lipid droplets in viral factories to support viral replication. Here, we assessed the antiviral activity of the direct pan-AMPK allosteric activator MK-8722 *in vitro.* MK-8722 efficiently inhibited infection of Alpha and Omicron SARS-CoV-2 variants in Vero76 and human bronchial epithelial Calu-3 cells at micromolar concentration. This inhibition relied on restoring the autophagic flux, which redirected newly synthesized viral proteins for degradation, and on a reduction in lipid metabolism, which affected the viral factories. Furthermore, MK-8722 treatment increased the type I interferon (IFN-I) response. Post-infection treatment with MK-8722 was enough to inhibit efficiently viral replication and restore the IFN-I response. Finally, MK-8722 treatment did not alter the SARS-CoV-2-specific $CD8^+$ T cell response mounted upon Spike vaccination. Overall, by activating AMPK, MK-8722 acts as an effective antiviral against SARS-CoV-2 infection, even when applied post-exposure, paving the way for preclinical tests aimed at inhibiting viral replication and improving patients' symptoms.

44 **INTRODUCTION**

45 The COVID-19 pandemic was efficiently contained due to the rapid development of vaccine and efficient
46 public health policies. However, despite these efforts, SARS-CoV-2 Variants Of Concern (VOC), which are
47 poorly sensitive to these vaccines, emerged and spread in the population, resulting in millions of deaths
48 [1]. Meanwhile, it has been challenging to develop an efficient antiviral treatment with an acceptable
49 benefit/risk ratio. As of January 2024, the treatment of patients in the intensive care unit (ICU) remains
50 primarily limited to drugs that either inhibit viral components such as Remdesivir and Paxlovid or target
51 SARS-CoV-2-induced cytokine storm, such as the IL-6 receptor antagonist Tocilizumab [1,2].

52 After its nasal entry, SARS-CoV-2 primarily infects lung epithelial cells in a mechanism by which the viral
53 envelope spike protein (Spike) binds to its main receptors angiotensin converting enzyme 2 (ACE2)
54 and/or transmembrane protease serine 2 (TMPRSS2). Following viral entry and the delivery of viral RNA
55 into the cytosol, the viral genes ORF1a and ORF1b are translated to the RNA-dependent RNA-
56 polymerase (RdRp). The viral RdRp further generates the remaining viral mRNA and the viral cycle
57 subsequently proceeds by hijacking cellular processes [2]. Replication of SARS-CoV-2, similar to other
58 enveloped RNA viruses, is supported by so-called viral factories with highly curved and three-
59 dimensional folded membrane extensions of modified endoplasmic reticulum [3,4], which formation
60 requires an increase in cell lipid metabolism. Viral factories compartmentalize viral genome from the
61 cytosol for replication and transcription, and provide protection against host cell defences. Disrupting
62 lipid metabolism hinders viral replication [5–7]. Accordingly, SARS-CoV-2 infection results in a significant
63 alteration in the cellular lipid repertoire in favor of polyunsaturated fatty acids, which are necessary for
64 the generation of infectious viruses [8–11]. This shift in lipid profile is mainly driven by the viral proteins
65 ORF9, nsp4 and nsp6, leading to the accumulation of lipid droplets in infected cells *in vitro* and in COVID-

66 19 autopsy tissues [5,12–15]. Accordingly, disrupting chemically either of these mechanisms inhibits SARS-
67 CoV-2 replication [5,11,12,14,16].

68 Throughout the SARS-CoV-2 viral cycle, autophagy is sequentially activated and inhibited [17–20]. Indeed,
69 autophagy is initiated by the early expressed nsp6, resulting in the formation of autophagosomes that
70 are essential for the establishment of viral factories [17,21] and subsequent viral proteins expression [17,21]. In
71 turn, viral proteins OFR3a and ORF7a expressed at latter time post-infection prevent the fusion between
72 autophagosomes and lysosomes thereby blocking completion of autophagy, as evidenced by increased
73 LC3-B expression, activation of the ULK1 kinase and increase in the autophagy cargo receptor
74 sequestosome-1/p62. Overall, this disruption of autophagy protects newly formed virus from
75 degradation in the LAMP1^{+} lysosome [19,22–25].

76 SARS-CoV-2 infection also impairs the expression of Interferon type 1 (IFN-I) and Interferon Stimulated
77 Genes (ISG), such as *Mx1* or *OAS1.* This reduction fails to restrict SARS-CoV-2 replication and this
78 contributes to the hyperinflammatory symptoms observed in COVID-19 [26–29]. Finally, SARS-CoV-2
79 infection interferes with the establishment of an efficient cellular response. By escaping lysosomal
80 degradation, SARS-CoV-2 limits viral peptide loading onto MHC-I and subsequent presentation to
81 specific cytotoxic CD8^{+} T Lymphocytes (CTL) [30,31]. In addition, SARS-CoV-2 ORF8 down-regulates MHC-I
82 expression from the plasma membrane, making infected cells less sensitive to SARS-CoV-2-specific CTLs
83 [32].

84 AMP-activated protein kinase (AMPK) is a highly conserved cellular energy sensor that plays a crucial
85 role in restoring the cellular energy balance by inhibiting ATP-consuming pathways (anabolism) and
86 activating ATP-producing pathways (catabolism) [33]. Notably, AMPK is a central regulator of lipid and
87 protein metabolism. AMPK inhibits fatty acid and cholesterol synthesis, by direct phosphorylation in S79
88 and resulting inhibition of acetyl-CoA carboxylase (ACC) and 3-hydroxy-3-methylglutaryl-CoA (HMG-CoA)

89 reductase [33]. Additionally, AMPK is vital for the regulation of protein synthesis and cell growth through
90 the inactivation of mTORC1 signalling through phosphorylation of Tuberous Sclerosis Complex 2 (TSC2)
91 and Raptor at position S792 [33]. Moreover, by activating Unc-51-like autophagy-activating kinase 1 (ULK1)
92 after phosphorylating S555 and stimulating Nuclear factor erythroid 2-related factor 2 (NRF2)-
93 dependent p62 increased expression, AMPK activation finely tunes cellular metabolic pathways [33]. AMPK
94 appears as a critical hub of cellular pathways affected by SARS-CoV-2 that are crucial for viral replication
95 and pathogenesis.

96 A multitude of indirect and direct AMPK activators have been tested in preclinical models in various
97 domains including viral infection and metabolic diseases [33–35]. Recently, MK-8722, a direct allosteric-
98 activator of AMPK, has been developed [36]. MK-8722 is effective *in vitro* in the micromolar range on
99 AMPK activation, compared to the millimolar range for metformin and 5-aminoimidazole-4-carboxamide
100 riboside (AICAR) [36,37]. MK-8722 has already been orally tested at 10 mg/kg in preclinical models of
101 diabetes, resulting in improvements of glycemia but with a minor and reversible cardiac hypertrophy [36].

102 Here, we investigated whether allosteric AMPK activation by MK-8722 inhibits SARS-CoV-2
103 infection/replication by promoting autophagy of viral particles and restoring normal lipid metabolism
104 and the IFN-I response.

105

106 **MATERIAL AND METHODS**

107 **Cell culture and chemical compounds**

108 All cells were cultured at 37°C in a humid atmosphere with 5% CO2. Vero76 (ATCC CRL-1587), Calu-3
109 (ATCC HTB-55) and Caco2 (ATCC HTB-37) cells were cultured in DMEM (Gibco 41966-029) containing 1%
110 Penicillin-Streptomycin (PS) (Gibco 15140122) and decomplemented Foetal Calf Serum (FCS) (Eurobio

111 CVFSVF06-01) at 10% (D10) for Calu-3 and Vero76 cells, and at 20% (D20) for Caco2 cells. Caco2 cells
112 culture medium was supplemented with 1% MEM Non-Essential Amino Acids (Gibco 11140035). All viral
113 inoculations and infections were made in DMEM containing 2% FCS (D2).

114 Peripheral blood mononucleated cells (PBMCs) of healthy donor were collected from the French blood
115 bank (Etablissement Français du Sang, EFS) after initiation of SARS-CoV-2 vaccination in the global
116 population (June 2021). PBMCs were obtained by Ficoll gradient centrifugation, aliquoted and stored in
117 StemMACS CryoBrew (Miltenyi, 130-109-558) until use. $CD8^+$ T cells were isolated from HLA-$A2^+$
118 individuals using CD8 microbeads (Miltenyi 130-045-201) following manufacturer instructions. Cells
119 ($5x10^6$ cells at 10^6 cells/mL) were further expanded with TransAct (Miltenyi, 130-111-160, 1:100 dilution)
120 for 15 days in RPMI 10% FCS, 2 mM L-Glutamine (R10) (Thermo 25030081) + 10 IU/mL IL-2 (Roche
121 11011456001) after CD3/CD28 stimulation. TransAct was then washed out and cells frozen (1 million
122 cells/vial) as described above. CD14-depleted PBMCs from healthy donors were obtained by collecting
123 the flow-through of CD14 magnetic isolation (Miltenyi, 130-050-201). Resulting cells were then frozen as
124 described above.

125 The absence of Mycoplasma in the cell lines was routinely controlled using the MycoAlert mycoplasma
126 detection kit (Lonza, LT07-318).

127 Remdesevir and MK-8722 were purchased at MedChemExpress (respectively HY-104077 and HY-
128 111363) and solubilized in DMSO at 10 µg/mL.

129

130 **Virus Propagation**

131 SARS-CoV-2 variant Alpha and Omicron were obtained as we described [38,39], viral stocks prepared by
132 amplification on Vero76 cells as we described [35,], aliquoted and cryopreserved at -80°C. Viral stocks were
133 titrated on Vero76 cells after thawing as we described [35].

134

135 **Foci Forming Assay**

136 Hundred thousand of Vero76 cells were seeded in 48 well-plates one day before infection, resulting in
137 confluent cells at the day of infection. Virus-containing supernatant from infected cells to be tested
138 were diluted at least 1,000 times in 100 µl of D2 and added to cells for 2h and then replaced with an
139 overlay medium (300 µl) composed of 0.3% Low Melting Agarose (Sigma A0701) in D2 at 37°C. Plates
140 were then placed at 4°C for 10 min to allow overlay medium to solidify and further incubated for 18h at
141 37°C. Plates were washed 3 times with PBS (Gibco 25300) to remove overlay, fixed with 4%
142 paraformaldehyde (PFA) (Electron Microscopy Sciences 15710) in PBS (PBS-4% PFA) for 1h at room
143 temperature and permeabilized with 0.1 % Triton-X100 in PBS for 10 min. Cells were washed 3 times
144 and the viral nucleocapsid was labelled using an biotinylated-anti-N-antibody at 300 ng/mL (Bioss bsm-
145 41411M-biotin) in PBS supplemented with 0.1% Saponin (Sigma S-7900), 2% FCS, and 2 mM EDTA (Perm
146 Buffer) for 30 min at room temperature. Cells were washed three times in PBS, incubated with
147 streptavidin-coupled-HRP 0.1 µg/mL (Vector Laboratories, INC, Burlingame, CA, 94010) in Perm Buffer
148 for 30 min, washed again, and incubated with 100 µl/well of KPL TMB TrueBlue (Sera Care 5510-0030)
149 for 30 min at 37°C.

150 The infectious index was established as the ratio of the viral copy number/mL over the FFU/mL titre
151 computed from paired datasets obtained in RT-qPCR and titration experiments.

152

153 **Inhibition assay**

154 Vero76 and Calu-3 cells were plated respectively at least 1 and 5 days before infection. Cells were
155 treated with MK-8722 either continuously or only after infection (post-infection). Continuous treatment
156 consisted in treatment at indicated concentrations for 1h before infection at 37°C, during the 2h
157 inoculation, and until endpoint. Fully confluent cell layers were infected with an MOI of 0.001 for Vero76
158 cells or of 0.05 for Calu-3 in D2 for 2h. Inoculates were replaced by fresh D2 containing or not MK-8722,
159 and cells further incubated for 1 and 4 days for Vero76 and Calu-3 cells, respectively. Before harvesting
160 cells, supernatants were collected, clarified by centrifugation, and stored at -80°C for further RT-qPCR
161 quantification and viral titration.

162 When indicated, untreated or pre-treated cells with 1 µM or 5 µM MK-8722 (for Vero76 and Calu-3 cells,
163 respectively) were inoculated at 4°C for 1h to allow virus attachment to the cell membrane, wash three
164 times in ice cold PBS and fresh D2, with or without MK-8722, was added before rising the temperature
165 to 37°C for 1h or 24h for Vero76 and for 32h for Calu-3 cells, as indicated. Cells were then harvested and
166 processed for *N* RNA quantification as described below. For post-infection treatments, MK-8722 was
167 added at 8h post-infection (hpi) or 1 day post-infection (dpi), to reach indicated concentrations, controls
168 receiving the same volume of D2.

169

170 **Quantification of infection by flow cytometry**

171 Single-cell staining for viral protein and RNA by FISH-Flow was performed as described [38].

172 Briefly, cells were detached with trypsin 0.05% (Gibco 25300-024) for 10 min at 37°C and placed in 96
173 wells-plates. After centrifugation, cells were stained for 5min on ice for viability (Viobility 405/452,
174 Miltenyi 130-130-420, diluted 100 times in cold PBS). Cells were washed in PBS and fixed with PBS-4%

175 PFA. Cells were washed in Perm Buffer and labelled for 30min with anti-spike-AF488 antibody (R&D
176 FAB105403G) diluted 250-fold in Perm Buffer and washed in Perm Buffer.

177 To further label viral RNA, cells were washed twice in Hybridization Wash Buffer (HWB) (2X SSC, 10%
178 formamide (MP Biomedicals FORMD002), 0.2 mg/mL Bovine Seric Albumin (BSA) UltraPure
179 (ThermoFisher Scientific AM2618) in ultrapure water (Invitrogen 10977-035)), resuspended in
180 hybridization buffer (10% (w/v) Dextran sulfate (Calbiochem 265152), 1 mg Yeast tRNA (Invitrogen
181 AM2616), 2X SSC, 10% Formamide, 0.2 mg/mL BSA RNase-free in ultrapure water) with 50 nM total
182 SARS-CoV-2-quasar670-specific FISH probes (Stellaris) in equimolar proportion, targeting regions of S,
183 ORF1 and N genes, resuspended in hybridization buffer and incubated for 12-16h at 37°C. After three
184 washes in HWB, cells were resuspended in PBS and analysed by flow cytometry. Proportion of infected
185 cells was quantified by flow cytometry (Guava 12-HT flow cytometer, Millipore) and analysed using the
186 native GuavaSoft 3.4 software.

187

188 **Western-blotting**

189 Cells were washed 3 times in PBS and lyzed with 1% Triton X-100 in 50 mM Tris pH 7.4, 150 mM NaCl, 1
190 mM EDTA, 1 mM EGTA, 10% Glycerol, 1 mM DTT, 1% Proteases Inhibitor Cocktail (Sigma P8340), 1%
191 Phosphatases inhibitor cocktail II and III (Sigma P5725 et P0044 respectively). Cell lysates were clarified
192 by centrifugation at 15,000g for 10min at 4°C, aliquoted and stored at -80°C. Protein content was
193 quantified by BCA assay after sample thawing (Thermo Fischer J61522.AP). Around 25µg protein were
194 separated by SDS-PAGE 12% at 100 mV and transferred on nitrocellulose membranes in wet condition at
195 80 mA at 4°C for 3h. Membranes were then saturated with TBS-0.5% Tween-20 (Sigma P1379, TBS-T)-5%
196 BSA. After three washes in TBS-T, membranes were incubated with primary antibodies described in
197 table 1 for 16h at 4°C. After three washes in TBS-T, relevant secondary antibody conjugated to HRP (see

198 **Table 1**) was added for 1h at room temperature followed by washed 3 times in TBS-T. Finally,
199 membranes were incubated with the West PicoPlus ECL HRP substrate (Thermo Fischer 34580). Signal
200 was imaged with Fusion FX (Villber Lourmat) and quantified using Fiji ImageJ software. When indicated,
201 data were computed from the Log2 fold change of the condition of interest over Non-infected non-
202 treated cells and presented as heat map using GraphPad8.

203

Table 1: Antibody list used for western-blotting

Target	Host and antibody nature	Conjugation	Supplier & reference	Dilution
β-actin	Goat polyclonal	-	Abcam ab8229	4,000
p-Thr172-AMPK	Rabbit polyclonal	-	CST 2531	5,000
Pan-AMPK	Rabbit polyclonal	-	CST 2532	5,000
p-Ser79-ACC	Rabbit polyclonal	-	CST 11818	5,000
Pan-ACC	Rabbit polyclonal	-	CST 3676S	5,000
p-Ser555-ULK1	Rabbit polyclonal	-	CST 5869	5,000
Pan-ULK1	Rabbit polyclonal	-	CST 4773	5,000
p-Ser792-Raptor	Rabbit polyclonal	-	CST 2083	5,000
Nucleocapsid	Mouse IgG2b	Biotin	BIOSS bsm-41411M-biotin	3,000 (300 ng/mL)
Pan-Raptor	Rabbit polyclonal	-	CST 2280	5,000
SQSTM1/p62	Rabbit polyclonal	-	CST 5114	5,000
Goat	Monkey polyclonal	HRP	Promega V805A	5,000
Rabbit	Donkey polyclonal	HRP	Southern Biotech 6440-05	5,000
Streptavidin	-	HRP	Vector Laboratories, INC, Burlingame, CA, 94010	10,000

204

205 **RNA extraction, N normalizer plasmid and RT-qPCR**

206 For RNA extraction, cells were washed 3 times in PBS and lysed in RA1 buffer. RNA was then extracted
207 using Nucleospin RNA kit (Macherey-Nagel 740955) following manufacturer instructions, and stored at -
208 80°C before RT-qPCR experiments. Primers and probes, designed according to original CDC
209 recommendations[40], are described in **Table 2** (Eurofins Genomics). Normalizer plasmid was obtained
210 after T-A cloning of the corresponding cDNA using High-Capacity RNA-to-cDNA kit (Thermo Fischer
211 387406) amplified using regular N-directed PCR with Platinium Taq (Thermo Fischer 10966034) following
212 the TOPO cloning kit instruction (Thermo Fischer 10966034) and transformation of homemade
213 thermocompetent TOP10 bacteria. Clones were selected using white-blue screening on LB agar plates
214 with 100 µg/mL ampicillin and 20 µg/mL X-Gal (Thermo Fisher R0941). Plasmids were extracted using
215 NucleoSpin Mini kit (Macherey Nagel 740588) and controlled by Sanger sequencing (Eurofins Genomics).
216 For *Nucleocapsid* RNA relative or absolute quantification, RT-qPCR was performed using 4µl of cellular
217 RNA and Taqman RNA-to-Ct 1step kit (Thermo Fischer 4392938) following manufacturer
218 recommendations using a LightCycler 480 (Roche). For IFN-I and ISG expression analysis, reverse
219 transcription was first carried out using High-Capacity RNA-to-cDNA and further quantified using Sybr
220 Master mix I (Roche #04707516001). Relative gene expression over *β-actin* in cell lysates was calculated
221 by the $2^{-\Delta\Delta Ct}$ method while absolute *N* abundance in supernatants was quantified using the N normalizer
222 plasmid.

Table 2: Primer characteristics

Target	Name	Sequence	Tm (°C)
Nucleocapsid	N2-Fow	TTACAAACATTGGCCGCAAA	53.2
	N2-Rev	GCGCGACATTCCGAAGAA	56
	N2-Probe	ACAATTTGCCCCCAGCGCTTCAG	64.2
β-Actin	βAct-Fow	TGTTTGAGACCTTCAACACC	55.3
	βAct-Rev	ATGTCACGCACGATTTCC	53.7
	βAct-Probe	CCTCACCGAGCGCGGCTACAGCTTCA	72.9
IFN-α	IFN-α Fow	ACAACCTCCCAGGCACAAGGGCTGTATTT	72.5
	IFN-α Rev	TGATGGCAACCAGTTCCAGAAGGCTCAAG	71.2
IFN-β	IFN-β Fow	GTTCCTTAGGATTTCCACTCTGACTATGGTCC	68.6

	IFN-β Rev	GAACTTTGACATCCCTGAGGAGATTAAGCAGC	68.6
Mx1	Mx1 Fow	CTGGTGCTGAAACTGAAGAAAC	60.8
	Mx1 Rev	TACCTCTGAAGCATCCGAAATC	60.9
OAS1	OAS1 Fow	TCCACCTGCTTCACAGAACTACA	64.5
	OAS1 Rev	GGCGGATGAGGCTCTTGAG	63

223

224 **Immunofluorescence**

225 Calu-3 cells were plated on Poly-L-Lysine (Sigma P8920) (0.1% in H_20) coated Ibidi slides (Ibidi 80841) at
226 $1.2x10^5$/well for 5 days and infected with SARS-CoV-2 as described above. At 3dpi, cells were washed,
227 stained with 10 µg/mL Nile Red (Sigma 72485) in PBS at 37°C for 20 min, and washed prior fixation,
228 when indicated. Cells were fixed in PBS-4% PFA for 1h, washed and permeabilized using 0.1% TritonX-
229 100 in PBS for 10 min. Non-specific binding was blocked with 5% FCS in PBS for 30 min. Cells were
230 further labelled in Perm Buffer with biotinylated-anti-N antibody at 300 ng/ml (BIOSS bsm-41411M-
231 biotin) and/or anti-LAMP1 at 625 ng/mL (BD 555798), or anti-LC3b antibody at 1 µg/mL (Novus
232 Biological, #NB600-1384SS) and anti-LAMP1 antibody at 625 ng/mL, overnight at 4°C and the relevant
233 secondary for 1h at room temperature (Streptavidin-AF488 Invitrogen S11223 at 2 µg/mL final, anti-
234 mouse IgG1-Cy5 Abcam ab136127 at 1.5 µg/mL final or anti-Rabbit-Cy3 IgG at 1 µg/mL, Jackson 711-
235 166-152, and anti-mouse IgG1-Cy5 at 1.5 µg/mL). After nuclear staining with DAPI, cells were washed,
236 and slides mounted with Ibidi mounting medium (Ibidi 50001). Staining was observed by confocal
237 microscopy (Xplore confocal microscope). At least five randomly chosen fields per condition were
238 imaged and further analysed using ImageJ software and the particle analysis function. Lipid droplets (LD)
239 were identified as Nile Red positive vesicular objects with diameter > 500 nm. Lysosomes were
240 identified as LAMP1 positive vesicular objects with diameter > 700 nm. Analyse of lysosomes and LD was
241 performed using Z-projections made from 6 consecutive slices 300 nm apart. The number of particles
242 per infected cells, their mean area and intensity were then calculated. Colocalization on z-stack images
243 was analysed with the JACoP plugin using object-based colocalization and setting threshold at 137, 134

244 and 120 for Lysosomes, LD and nucleocapsid objects, respectively. Manders' Overlap Coefficients (MOC)
245 corresponding respectively to green objects colocalizing in red objects and inversely red objects
246 colocalizing in green objects were computed.
247
248 **Lysosomal function analysis**

249 Confluent Calu-3 cells in a 96-well plate were inoculated with either Alpha or Omicron variant at 0.05
250 MOI for 2h, and cells were further cultured with fresh D2 up to 24hpi. MK-8722 at indicated
251 concentration or D2 only were added for another 24h. Lysosomes were then stained with 5 nM
252 Lysotracker RED DND-99 (ThermoFischer L7528) in DMEM for 30 min following the manufacturer
253 instructions. Cells were then detached with trypsin 0.05% for 10 min, transferred into round bottom
254 96well-plate, stained for viability and fixed with PBS-4% PFA. After 20 min, cells were washed and the
255 mean intensity of Lysotracker staining was quantified by flow cytometry as described above.
256
257 **Evaluation of MK-8722 treatment on T cell activation**

258 CD14-depleted PBMCs were thawed and cultured overnight at 37°C in R10 supplemented with 10 UI/mL
259 IL-2 and 1 µg/mL DNAse (StemCell, 07900). Cells were then washed, resuspend cells in R10 and
260 distributed at 10^5 cells/well in a round bottom 96-well plate. Transact stimulation, which is a
261 combination of activating anti-CD3 and anti-CD28 antibodies (Miltenyi, 130-111-160), consisted in 100-
262 fold final dilution of Transact in R10. Alternatively, Spike or Nucleocapsid Peptivator, T cell epitope
263 peptide pools from either Spike or Nucleocapsid of SARS-CoV-2, respectively (Miltenyi 130-126-700 and
264 130-126-698, respectively) was used as stimulation source at a final concentration of 500 ng/mL in R10.
265 After stimulation for 30 min, Brefeldin A (5 µg/mL final) containing anti-CD107a-PE-Cy5 antibody (BD
266 555802) following the manufacturer instruction was added and cells were incubated for 6h. Cells were

267 then washed and stained with anti-CD3-APC-H7 (BD 560176) and anti-CD4-APC (BD 551980) following
268 manufacturer instructions for 10 min on ice, followed by viability staining as described above and
269 fixation in PBS-4% PFA. Cells were further stained overnight with anti-IFNγ-PE (Miltenyi, 130-113-498)
270 following manufacturer instructions in Perm Buffer. Cells were washed in Perm Buffer and then in PBS.
271 Frequencies of $CD4^+$ and $CD8^+$ T cells expressing $CD107a^+$ or $IFN\gamma^+$ were quantified by flow cytometry as
272 described above. For each donor, we determined the net activation (NA) level for each marker after
273 stimulation with Peptivator (NA(Peptivator)) by normalizing CD107a and IFNγ frequencies measured
274 after stimulation with Peptivator over those measured after stimulation with Transact. This activation
275 index reflects the capacity of the donor cells to respond to peptide-specific stimulation relative to its
276 intrinsic stimulatory capacities.

277

278 **Evaluation of combined antiviral effects of MK-8722 and $CD8^+$ T cells from vaccinated individuals on**
279 **epithelial cell infection**

280 $CD8^+$ T cell activation being restricted to MHC-I, antigenic presentation occurs only between as antigen
281 presenting cell (i.e. infected cell) and the T cells with similar HLA. We first showed that Caco2 cells,
282 unlike Calu-3 cells, express the MHC-I molecule HLA-A2 and were thus capable of presenting antigens to
283 HLA-A2-restricted CD8+ T cells from vaccinated individuals. Therefore, confluent Caco2 cells were
284 inoculated for 1h with SARS-CoV-2 and further incubated for 8h in the absence of virus. Previously
285 amplified $CD8^+$ T cells were thawed in R10 complemented with 5IU/mL IL-2 to promote T cell survival,
286 washed and added to Caco2 cells at 8hpi with or without 2.5 or 5 µM MK-8722. The co-cultures were
287 further incubated at 37°C for 36h. T cells were then collected, stained with anti-CD3-APC-H7 (BD
288 560176) and anti-CD8-APC (BD 345775) following manufacturer instructions, and for viability before

289 fixation as above. Cells were then intracellularly stained with anti-spike-AF488 (R&D FAB105403G) for 1h
290 at room temperature. Infection was monitored in $CD3^{-}CD8^{-}$ cells by flow cytometry as described above.

291

292 **Graphical representation and statistics**

293 Data and graphs were computed using Graphpad Prism (San Diego, V8). If variables followed a normal
294 distribution after Shapiro-Wilk, *t*-test or ANOVA was calculated; otherwise, statistical analyses were
295 performed using the Mann-Whitney or Kruskal-Wallis test. *p*-values <0.05 were considered significant.
296 Tests were paired when experience design permitted.

297

298 **RESULTS**

299 ***MK-8722 inhibits SARS-CoV-2 replication in epithelial cells.***

300 We first evaluated the activity of the pan-AMPK allosteric activator MK-8722 in Vero76 cells. As early as
301 1h after treatment, MK-7288 activated AMPK and triggered downstream phosphorylation of ACC in a
302 concentration dependent manner from 0.01 to 1 µM (**Fig. S1**). The antiviral activity of MK-8722 was then
303 monitored in Vero76 cells infected by SARS-CoV-2 as schematized (**Fig. 1A**). The drug was added at 0.01
304 to 1 µM to the cells 1h before infection, during the inoculation with SARS-CoV-2 Alpha for 2h, and during
305 the subsequent 24h chase. At 1dpi, Spike expression was quantified by flow cytometry (see gating
306 strategy **Fig. S2A**). $Spike^{+}$ cell frequency decreased in the presence of MK-8722, from 11.8±0.7% in
307 untreated to 5±0.4% in 1 µM-treated conditions (ANOVA: p<0.001, **Fig. S2B**), corresponding to an
308 inhibition of infection of 53±3% at 1 µM (ANOVA: p<0.0001, **Fig. 1B**). MK-8722 antiviral activity was
309 further analysed in bronchial Calu-3 cells (See gating strategy **Fig. S2C**), which are more relevant to
310 SARS-CoV-2 infection since they express TMPRSS2 and are competent for IFN-I signalling similar to

311 bronchial cells *in vivo* unlike Vero76 cells. Infection of Calu-3 cells with alpha variant in the presence of
312 MK-8722 significantly decreased the frequency of viral Spike$^+$ and viral RNA$^+$ cells in a dose-dependent
313 manner compared to untreated cells (**Fig. S2D**). At 10 µM MK-8722, the frequency of Spike$^+$ and viral
314 RNA$^+$ cells decreased compared to untreated cells, from 30.8±2.5% to 3.6±0.2%, and from 15.1±1% to
315 1.5±0.2%, respectively (ANOVA: $p<0.0001$, **Fig. S2D**). MK-8722 similarly inhibited Omicron infection, the
316 frequency of Spike$^+$ and viral RNA$^+$ cells decreasing compared to untreated cells (compare 27.5±3%
317 versus 4.5±0.6% Spike+ cell frequency and 31±3% vs 4.5±0.4% RNA+ cell frequency at 10 µM and
318 without MK-8722, respectively) (**Fig. S2E**). These reductions were comparable to that induced by
319 treating Calu-3 cells with the RNA-dependent RNA polymerase inhibitor Remdesivir at 1 µM (**Fig. S2F**).
320 The IC50 of MK-8722 in Calu-3 cells against Alpha variant was reached at 0.7 µM and an IC90 at 9 µM (*t*-
321 test: $p<0.05$, **Fig. 1C**). For the Omicron variant, MK-8827 showed an IC50 at 1,6 µM and an IC90 slightly
322 above 10 µM (ANOVA: $p<0.05$, **Fig. 1D**). Both RNA$^+$ and Spike$^+$ frequencies decreased after MK-8722
323 treatment. As MK-8722 antiviral activity against Alpha and Omicron variants is similar, the drug likely
324 targets the same pathways in the two cases. Furthermore, MK-8722 blocked viral production by Calu-3
325 cells in a concentration-dependent manner, as quantified by the decrease in *N* RNA by RT-qPCR from
326 $1.5\pm0.14\times10^9$ to $6\pm1.4\times10^7$ viral copies/mL at 10 µM MK-8722 (ANOVA: $p<0.0001$) (**Fig. 1E**). MK-8722 did
327 not alter the expression of ACE2 in Vero76 and Calu-3 cells, as measured by flow cytometry (**Fig. S2G**),
328 nor impacted cell viability (**Fig. S2H**), indicative of a post-entry antiviral activity. Furthermore, we also
329 investigated MK-8722 toxicity at 4h, 24h and 96h (Fig. S2I) and found that the drug was not toxic up to
330 10µM. The 50% toxicity dose was calculated to be 57µM at 96h in Calu3 cells. This allows us to
331 determine a therapeutic index of 76 against the SARS-CoV-2 Alpha variant and 36 against the Omicron
332 variant, thus, placing MK-8722 as an attractive antiviral candidate.

333 We next investigated whether MK-8722 exerts its antiviral effect at the early infection steps. After MK-
334 8722 pre-treatment of Vero76 and Calu-3 cells (at 1µM and 5µM, respectively), cells were inoculated

335 with Alpha or Omicron variants for 1h at 4°C to allow virus attachment. After virus removal, cells were
336 incubated in the presence of the drug at 37°C to synchronize infection. Viral *N* RNA was quantified by
337 RT-qPCR in the cells after a short (1h) or long (24h in Vero76 and 32h in Calu-3 cells) chase times. As
338 control, cells were similarly infected but left untreated. Viral RNA accumulated after 1h chase in the two
339 cell types for the two variants similarly in treated and non-treated conditions, although the drug had
340 tendency to decrease relative *N* RNA levels in a non-significant statistical manner (1±0.12 vs 0.82±0.08
341 for Vero76, 1±0.05 vs 0.91±0.15 and 1±0.1 vs 0.8±0.08 for Alpha and Omicron variants in Calu-3 cells,
342 respectively, *t*-test: ns in all conditions, **Fig. 1F** and **1G**). In contrast and as expected, *N* RNA expression
343 was significantly reduced after a longer chase (1±0.09 vs 0.52±0.12 for Vero76, 1±0.11 vs 0.2±0.04 and
344 1±0.1 vs 0.03±0.003 for Alpha and Omicron variants in Calu-3 cells, respectively, *t*-test $p<0.05$, <0.0001
345 and <0.0001, respectively). These results suggest that MK-8722 has little antiviral effect during the early
346 steps of infection, namely adsorption and fusion, but acts in a mechanism controlling post-entry
347 replication steps.

348

349 ***Post-infection treatment with MK-8722 is sufficient to inhibit SARS-CoV-2 replication.***

350 We next evaluated if MK-8722 was also active on cells after infection (**Fig. 1H**). Post-exposure treatment
351 at 1dpi and until harvest at 3dpi efficiently blocked viral replication, quantified by Spike expression, by
352 36±7% (**Fig. 1I**, ANOVA: $p<0.0001$), although still less than the continuous treatment, which reduced
353 infection by 63±6% (ANOVA: $p<0.0001$). Continuous and post-exposure treatment with MK-8722 (5 µM)
354 resulted in a similar inhibition of viral genomes accumulation of both Omicron and Alpha variants in
355 infected cells (**Fig. 1J**). Indeed, after continuous treatment with MK-8722 for 34h, *N* RNA relative amount
356 decreased significantly by 80±0.04% and by 97±0.7% in Alpha and Omicron infected cells, respectively (*t*-
357 test: $p<0.0001$ for both variants vs untreated cells). Limiting the MK-8722 treatment to the post-

358 exposure phase, namely from 8hpi, decreased *N* RNA relative amount by 75±0.05% and 80±20% in Alpha
359 and Omicron infected cells, respectively (ANOVA: $p<0.0001$ for both Alpha and Omicron variants vs
360 untreated cells). Altogether, these data suggest that post-exposure treatment by MK-8722 is sufficient
361 to inhibit viral infection.

362

363 ***MK-8722-induced AMPK activation triggers autophagy induction and inhibits lipids metabolism to***
364 ***control SARS-CoV-2 replication.***

365 We further examined the mechanism of SARS-CoV-2 inhibition by MK-8722. Therefore, the modification
366 by the drug of the signalling cascade downstream AMPK activation during SARS-CoV-2 infection of
367 Vero76 and Calu-3 cells relative to no treatment was analysed using western blot (**Fig. S3A-B**).
368 Quantification of the western blots relative to non-infected non-treated control condition is shown in
369 **Fig. 2A** and summarized in a heat map in which values were expressed as log2 fold change (Log2(FC))
370 (**Fig. 2B**). As expected, MK-8722 treatment of both Vero76 and Calu-3 cells significantly activated AMPK
371 that became phosphorylated at position S172 (0.85±0.4 and 1.2±0.3 log2(FC), t-test: $p<0.05$ and $p<0.01$,
372 respectively, **Fig. 2B**). AMPK phosphorylation was comparable in infected and non-infected cells (0.0±0.5
373 and -0.02±0.3 log2(FC), respectively), while MK-8722 treatment stimulated AMPK phosphorylation even
374 more in infected than in non-infected cells (3.1±0.4 and 2.3±0.9 log2(FC), respectively, t-test: $p<0.05$
375 both). As expected, the drug blocked infection as shown by a significant decrease in N protein levels in
376 both Vero76 and Calu-3 cells (-0.88±0.2 and -1.7±0.4 Log2(FC), respectively, t-test: $p<0.05$ both, **Fig. 2A-**
377 **B**).

378 We then monitored S555 ULK1 phosphorylation and p62 relative expression as markers of the initiation
379 of autophagy, Raptor phosphorylation as a marker of protein synthesis inhibition, and S79 ACC
380 phosphorylation as a marker of the disruption of lipid metabolism. While neither MK-8722 nor SARS-

381 CoV-2 infection alone affected ULK1 phosphorylation (with the exception of Calu-3 cells, non-infected
382 but treated, where increase reached 1±0.2 Log2(FC), $p<0.01$), MK-8722 treatment during infection was
383 associated with an increase in ULK1 S555 phosphorylation in both cell types (from 0.05±0.5 to 2.8±1.2
384 Log2(FC) in Vero76 cells and from -0.9±0.5 to 1.3 ±0.6 Log2(FC) in Calu-3 cells, t-test: ns and $p<0.05$,
385 respectively, **Fig. 2A-B**). Concomitantly, p62 expression strongly and significantly increased in both cell
386 types (3.33±0.56 and 2±0.6 Log2(FC) for Vero76 and Calu-3 cells, respectively, t-test $p<0.05$, **Fig. 2A-B**).
387 S792 Raptor phosphorylation remained unchanged whatever the conditions. Finally, SARS-CoV-2
388 infection strongly decreased S79 ACC phosphorylation significantly (-1±0.29 and -0.7±0.2 Log2(FC),
389 respectively and *t*-test: $p<0.05$, **Fig. 2A-B**) while it was significantly increased by MK-8722 treatment
390 during infection (1.9±0.5 and 1±0.2 Log2(FC), *t*-test: $p<0.05$ and $p<0.01$, respectively, **Fig. 2A-B**).

391 Altogether these results suggest that the antiviral mechanism of MK-8722 relies on the AMPK activation-
392 dependent restoration of the autophagic flux that is otherwise blocked by SARS-CoV-2 proteins, due to
393 ULK1. Phosphorylation of ULK1 and increased p62 expression likely result in an increased access of viral
394 components to phagosomes and further phagosomes fusion with lysosomes, resulting in subsequent
395 degradation of viral proteins in phagolysosomes, preventing viral dissemination. As complementary anti-
396 viral mechanism, MK-8722 treatment increases ACC phosphorylation that decreases lipid synthesis,
397 which may reduce lipid droplets content and thus affect the establishment of viral factories. However,
398 as shown by the lack of Raptor phosphorylation, the antiviral activity of MK-8722 does not involve a
399 shutdown of viral protein synthesis. Trends in all marker changes after MK-8722 treatment were similar
400 between cell lines indicating a common antiviral mechanism. We therefore focused our study on Calu-3
401 cells since they are more relevant to SARS-CoV-2 infection.

402

403 ***MK-8722 treatment perturbs the viral factory establishment.***

404 We next explored the capacity of MK-8722 to perturb the distribution of lipids associated with viral
405 factories and lipid droplets in cells infected with the Alpha variant. Therefore, lipid reorganisation in
406 infected Calu-3 cells was monitored after continuous treatment with MK-8722 by staining lipids with the
407 lipophilic marker Nile Red analysed by confocal microscopy. As expected [34], treatment with MK-8722 in
408 uninfected cells blocked almost entirely the synthesis of lipids, as shown by the loss of Nile Red staining
409 (**Fig. S4A**). Infection increased the overall Nile Red staining by 40±10% compared to non-infected cells
410 (**Fig. S4B**, ANOVA: $p<0.05$), but also dramatically modified Nile Red cellular distribution into aggregates
411 likely corresponding to lipid droplets (compare **Fig. 3A, S4B**). This overall infection-induced increase in
412 Nile Red staining was abolished by MK-8722 treatment (**Fig. S4B**, 0.943±0.14-fold change, infected non-
413 treated vs treated cells, ANOVA: $p<0.05$) and returned to untreated uninfected cell level. Furthermore,
414 in infected cell, identified by viral N protein labelling, MK-8722 significantly reduced the number, area
415 and intensity of lipids droplets (as defined in the method section) (**Fig. 3A** and **3B**, 0.29±0.09 and
416 0.28±0.1 and 0.33±0.15 fold-change over infected non-treated cells, *t*-test: $p<0.01$, $p<0.05$ and $p<0.05$,
417 respectively). We then evaluated if the N protein, a maker of virus replication in viral factories, was
418 redistributed out of lipid droplets by the drug. In the absence of MK-treatment, N protein and lipids
419 colocalized as expected, although partially, with Manders' Overlap Coefficient (MOC) being in the range
420 of previous reports [12]. This colocalisation decreased significantly in cells infected in the presence of MK-
421 8722, as indicated by lower MOCs for N protein in Nile Red (0.085±0.024 vs 0.01±0.005, Mann-Whitney
422 $p<0.001$) and for Nile Red in N protein (0.16±0.05 vs 0.027±0.01, Mann-Whitney $p<0.01$) in MK-8722
423 treated vs untreated infected cells (**Fig. 3A** and **3C**). Altogether, SARS-CoV-2 infection increases the
424 accumulation of lipid droplets with which viral components colocalise. MK-8722 treatment reverses
425 these effects, likely reflecting an alteration of cell lipid composition following increased ACC
426 phosphorylation, thus limiting the production of viral factories.

427 SARS-CoV-2 is an enveloped virus; therefore lipid metabolism modification alters the lipid composition
428 of the viral membrane, and in turn viral particles infectivity [5,7–11] We thus measured viral production by
429 infected Vero76 and Calu-3 cells by quantification of secreted viral nucleocapsid *N* RNA by RT-qPCR. In
430 line with the reduction of secreted viral *N* RNA in presence of the drug shown above (**Fig. 1E**), the level
431 of viral *N* RNA secreted by both infected cell lines was reduced by 10-fold upon continuous MK-8722
432 treatment (**Fig. 3D**, $2\pm0.8\times10^4$ vs $6\pm2\times10^2$ and $3.4\pm1.7\times10^7$ vs $2.3\pm1.2\times10^6$ RNA copies/mL for Vero
433 (upper) and Calu-3 cells (lower), respectively, *t*-test: $p<0.05$ for Vero76 and $p<0.01$ for Calu-3 cells).
434 Accordingly, the amount of infectious viruses released by infected cells titrated in foci forming assay was
435 statistically decreased by MK-8722 in Vero76 (from $3\pm0.3\times10^4$ to $5.8\pm1\times10^3$ FFU/mL) and Calu-3 cells
436 (from $2.6\pm0.5\times10^5$ to $5.5\pm1\times10^4$ FFU/mL, *t*-test: $p<0.05$ for both cell types, **Fig. 3E**).

437 We next calculated an infectious index of released particles (described in the method section), which
438 inversely correlates with virus infectivity. The drug reduced the frequency of newly produced infectious
439 viruses by both cell lines (infectious index: 0.41±0.11 vs 0.05±0.02 in Vero76 cells (Mann-Whitney
440 $p<0.05$), and 0.07±0.03 vs 0.007±0.003 in Calu-3 cells (Mann-Whitney $p<0.05$) in the presence and
441 absence of the drug) (The drug reduced the frequency of newly produced infectious viruses by both cell
442 lines **Fig. 3F**). This inhibitory effect of MK-8722 on the production of infectious particles could not be
443 explained by a direct inhibitory role of MK-8722 present in the culture media on foci formation. Indeed,
444 tested cell culture media (**Fig. 1B, S2B**) were highly diluted in the assay (at least 1,000 times)
445 corresponding to a MK-8722 concentration < 0.005 µM, which is far under the limit of efficacy of MK-
446 8722 in Vero76 cells. Furthermore, MK-8722 exposure was limited to the 2h inoculation. Our data
447 suggests that the lipid metabolism alteration induced by MK-8722 counteracts SARS-CoV-2 replication
448 and affects production and infectivity of released viral particles.

449

450 ***MK-8722 enhances lysosomal degradation of viral components to promote antiviral immunity.***

451 As antiviral mechanism, MK-8722 could contribute to restoration of the autophagic flux (**Fig. 2**), which
452 should result in targeting viral proteins to lysosomes. We first evaluated the lysosome distribution after
453 MK-8722 treatment in infected cells. As a lysosomal marker, we used LAMP1 and characterized its
454 distribution in infected Calu-3 cells upon MK-8722 treatment by immunolabelling and confocal
455 microscopy in infected (**Fig. 4A**) and non-infected cells (**Fig. S5A**). SARS-CoV-2 infection significantly
456 decreased LAMP1 relative expression in Calu-3 cells as expected (**Fig. 4A and S5A,** quantified in **Fig. S5B**
457 as 0.47±0.06-fold change, ANOVA: $p<0.05$). This decrease likely reduced LAMP1$^+$ lysosome size as
458 infection inhibits autophagosome-lysosome fusion[22,24,25]. MK-8722 treatment during infection
459 significantly restored LAMP1 relative expression to its level in non-infected non-treated condition
460 (1.15±0.11-fold change, ANOVA: $p<0.01$ compared to infected non-treated condition; **Fig. S5B**).

461 We then characterized LAMP1$^+$ lysosome parameters, as defined in the method section. MK-8722
462 significantly increased LAMP1$^+$ lysosome number, area and specific intensity, indicative of their
463 enhanced activity in infected cells, which were identified by the expression of viral N protein (**Fig. 4B**,
464 2.5±0.25 and 2.53±0.2 and 4.3±1.1-fold change over infected non-treated cells, *t*-test: $p<0.001$, $p<0.05$
465 and $p<0.0001$, respectively). When colocalization of viral N protein and LAMP1 was quantified in
466 infected cells, MK-8722 treatment resulted in higher MOC as compared to infected non-treated cells (N
467 protein in LAMP1 signal: 0.02±0.003 vs 0.05±0.004, Mann-Whitney $p<0.01$; and LAMP1 in N protein
468 signal: 0.021±0.006 vs 0.048±0.007, Mann-Whitney $p<0.05$, **Fig. 4C**). To assess directly the impact of MK-
469 8722 on the autophagic flux, Calu3 cells were infected by SARS-CoV-2 without and with MK-8722 (5uM),
470 double labelled with LC3b and LAMP1, and co-localisation of the two markers quantified (**Fig.4D, E**). MK-
471 8722 treatment, compared with no treatment, increased LC3b colocalization in the LAMP1
472 compartment as shown by the increase in MOCs in treated versus non treated infected cells (LAMP1
473 signal in LC3b signal 0.078±0.014 vs 0.01±0.006, Mann-Whitney $p<0.05$, and LC3b in LAMP1 signal

474 0.04±0.02 vs 0.015±0.007 Mann-Whitney p<0.05). These results indicate that MK-8722 restored the
475 autophagic flux that had been interrupted by SARS-CoV-2 infection in Calu3 cells.

476 Lysosomal activity was quantified after Lysotracker staining by flow cytometry in Calu-3 cells infected for
477 24h and treated with MK-8722 for an additional day. MK-8722 increased lysosomal activity similarly
478 after infection by both Alpha and Omicron variants (Lysotracker MFI: 286±12 and 289±9.6 in MK-8722
479 treated vs 253±34 and 251±6 in non-treated cells, respectively for each variant, ANOVA: p<0.05 at least,
480 **Fig. 4F**). This result indicates that MK-8722 restores the autophagic flux to address viral components to
481 the lysosome, where they are degraded.

482

483 **MK-8722 restores the INF I pathway**

484 The lack of type-I IFN response is a major immune parameter contributing to COVID19 disease [29,41,42].
485 Completion of autophagy will most likely result in the degradation of viral proteins, which escape RIG-I
486 sensing thereby restoring IFNα and IFNβ production and associated downstream ISG such as OAS1 and
487 Mx1. We thus investigated IFN-I response in infected Calu-3 cells after continuous or post-infection
488 treatment with MK-8722 (**Fig. 4G**). Compared to untreated condition, continuous and post-infection
489 treatment with MK-8722 increased *IFNα* mRNA expression by 100±38% and 140±58% (Kruskal-Wallis:
490 *p*<0.05 for both treatments), while that of *IFNβ* decreased by 73±5% and 45±11% for continuous and
491 post-infection treatment, respectively (Kruskall-Wallis: *p*<0.01 and ns respectively). Regarding *ISG* mRNA
492 expression, *Mx1* level increased by 1.46±0.12-fold and by 1.49±0.19-fold for continuous and post-
493 infection treatment, respectively (Kruskal-Wallis: <0.05 both, respectively), while *OAS1* mRNA
494 expression increased by more than 2-fold in all treated conditions (2.8±0.6-fold and 2.1±0.3-fold,
495 respectively, Kruskal-Wallis: *p*<0.01). Altogether, MK-8722 treatment, even if initiated post-exposure,

496 can drive early IFN-I expression and downstream ISG, which, by controlling infection, could limit severe
497 outcome in patients [26,27,29,41,43].

498

499 **MK-8722 *in vitro* treatment does not alter T cell response against SARS-CoV-2 in vaccinated individuals**

500 T cell response is crucial to control SARS-CoV-2 infection [44–46], and relies on metabolism reprogramming
501 of the effector cell. We therefore investigated the impact of MK-8722-mediated AMPK activation on the
502 T cell response using primary cells obtained from peripheral blood of healthy individuals. We found that
503 MK-8722 alone compared to DMSO at identical concentration did not activate T-cell from healthy
504 donors (**Fig. S6A-B**). We then investigated if MK-8722 exposure affected T cell responses upon TCR
505 engagement. Healthy donor PBMCs were stimulated with anti-CD3 and anti-CD28 (CD3/CD28, TransAct)
506 to mimicking TCR engagement, and treated with MK-8722 for 6h. Intracellular IFNγ$^+$ and CD107a$^+$
507 frequencies were then analysed in CD4$^+$ and CD8$^+$ T cells. As expected, CD3/CD28 stimulation increased
508 both IFNγ$^+$ and CD107a$^+$ frequencies in both CD4$^+$ and CD8$^+$ T cells (**Fig. 5A**, 5.6±1.5% and 7.5±1.9% vs
509 0.6±0.2% and 1.1±0.2% for CD4$^+$ T cells, and 4.9±1.5% and 2±0.3% vs 0.68±0.1% and 0.3±0.06% for CD8$^+$
510 T cells, for IFNγ$^+$ and CD107a$^+$ frequencies respectively, *t*-test: $p<0.05$ at least). The concentrations of
511 MK-8722 tested had no negative impact on the expression of activation markers, and even showed a
512 trend towards increased activation with MK-8722 treatment. These results indicate that MK-8722 does
513 not affect degranulation and IFNγ responses and is thus compatible with the establishment of a T cell-
514 dependent protective immune response.

515 We next tested whether MK-8722 altered antigen-specific T cell stimulation. As a surrogate of SARS-
516 CoV-2 antigen after infection, we used peptides covering the immunodominant sequence domains of
517 the SARS-CoV-2 Spike (Peptivator peptide pool (Miltenyi)) to stimulate CD14-depleted PBMCs and
518 measure IFNγ$^+$ and CD107a$^+$ frequencies in both CD4$^+$ and CD8$^+$ primary T cells. We defined an activation

519 index as the level of activation induced by the peptide pool relative to the corresponding Transact level.
520 For these experiments, cells were collected from healthy individuals after summer 2021 when most of
521 them had been immunized at least two times with spike-based SARS-Cov-2 vaccine and consequently
522 mounted a Spike-specific T cell response. Accordingly, Spike peptide-pool stimulated only $CD4^+$ T cell
523 response although in a limited manner (**Fig. 5B**, activation index: 6.6±0.8 for IFNγ and 1.4±0.3 for
524 CD107a, *t-test:* $p<0.01$ and $p<0.05$). As for CD3/CD28 stimulation, MK-8722 stimulation showed a trend
525 towards increase all the tested T cell responses although only CD107a activation index for CD4+ T-cells
526 was statistically higher after MK-8722 treatment (i.e. 6.6±0.8 vs 13.3±4.7 for 10 µM MK-8722, ANOVA
527 $p<0.01$). Stimulation of CD14-depleted PBMCs with a SARS-CoV-2 Nucleocapsid peptide pool gave similar
528 results, even though the peptide pool alone failed to activate a T cell response (**Fig. S6C**). These data
529 suggests that if used as a drug, MK-8722 will likely not prevent the establishment of a T cell- specific
530 response against SARS-CoV-2 *in vivo*.

531 We finally evaluated whether MK-8722 and SARS-CoV-2-specific $CD8^+$ T cells could cooperate to block
532 infection of mucosal epithelial cells. However, Calu-3 cells being HLA-A2 negative, they could not be use
533 to present viral antigen to HLA-A2+ CD8+ T cells. For this reason instead of Calu-3 cells, we used the
534 epithelial Caco2 cells competent for IFN responses, which expressed HLA-A2 (not shown) and are
535 susceptible to SARS-CoV-2 infection Therefore, $CD8^+$ T cells were obtained from HLA-$A2^+$ healthy donors
536 obtained after the summer 2021. Post-exposure treatment with MK-8722 inhibited infection of Caco2
537 cells in a dose dependent manner, as shown in **Fig. 5C** (by 32±3% and 54±6%, at 2.5 and 5 µM
538 respectively (ANOVA: $p<0.0001$ for both conditions, see **Fig. S7** for the gating strategy). In the presence
539 of $CD8^+$ T cells, infection of Caco2 cells was reduced by 19.8±5% (ANOVA: $p<0.01$). Moreover, the
540 combination of $CD8^+$ T cells with MK-8722 increased the inhibition of infection in a dose-dependent
541 manner (50±3% and 71±4% inhibition in the presence of CD8+ T cells and 2.5 or 5 µM MK-8722,
542 respectively) compared to the inhibition of infection in the sole presence of CD8+ T cells (19.8±5%

543 ANOVA: $p<0.0001$ both, respectively) and in the presence of MK-8722 only (32±3% and 54±6% in the
544 presence of 2.5 or 5 µM MK-8722, *t*-test $p<0.05$ and ns for 2.5 and 5 µM, respectively) although no
545 synergy was observed. Altogether, our results confirm that MK-8722 treatment does not impair the
546 SARS-CoV-2-specific $CD8^+$ T cell-mediated response against mucosal Caco2 cell infection, but rather that
547 both act in combination to reduce cell infection.

548

549 **DISCUSSION**

550 To date, antivirals against SARS-CoV-2 infection without significant side effects have yet to be
551 characterised. Here, we provide evidence that the direct pan-AMPK allosteric activator MK-8722 is a
552 strong antiviral drug candidate against SARS-CoV-2 infection, as treatment with MK-8722 in the µM
553 range reduces infection of lung cells without altering the cellular immune response.

554 Previous studies have suggested that AMPK activation could inhibit viral infections [34], as viral infection
555 prevents AMPK activity. In the case of SARS-CoV-2 infection, AMPK activity is reduced and furthermore,
556 autophagy is blocked [18], while inhibition of either AMPK by Compound C or ULK1 by MRT68921
557 increases viral particle release [18,47]. We show here that the blockade of AMPK activation upon infection
558 can be reversed by MK-8722, the pharmacological allosteric pan-activator of AMPK, which blocks
559 infection at a µM concentration, in agreement with the predicted role of AMPK activity on SARS-CoV-2
560 infection[48] and with MK-8722 action on infection by other viruses[49].In line, metformin, a drug approved
561 by FDA since 1994, and the adenosine analogue AICAR that activates AMPK indirectly can inhibit
562 replication of SARS-CoV-2 as well as Flaviviruses, but at a concentrations of 10 and 1 mM, respectively
563 [35,47]. These AMPK-sensitive viruses replicate all in viral factories, disturbing lipid synthesis and escaping
564 autophagy [50,51]. AMPK activation by metformin at high concentration (10mM) inhibit SARS-CoV-2
565 replication in vitro [47]. However, AMPK activation with 5-amino-imidazolecarboxamide riboside (AICAR), a

566 non-metabolised analogue of AMP able to activate AMPK, used at 25 µM is unable to inhibit SARS-CoV-2
567 infection [18] while at 1 mM has been proven to reduce by 10-fold viral [47] suggesting that AMPK needs to
568 reach an activation threshold to inhibit viral replication. Conversely, NUAK2, an AMPK-related kinase,
569 was reported to stimulate viral replication in A549 and Calu3 cells [52]. Altogether our results, in
570 agreement with the literature, indicate that AMPK-dependent antiviral activity is restricted to AMPK-
571 members only, confirming their distance with AMPK-related kinases such as NUAK2 [53]. Despite
572 observational data suggesting an association between metformin use and prevention of severe COVID-
573 19 outcomes, metformin did not significantly lower risk of hospitalization and mortality due to SARS-
574 CoV2 infection in recent randomized controlled trials [54]. Furthermore, in vivo, metformin mainly targets
575 the liver and the gastrointestinal tract [55] and therefore could have limited effect in the upper airway, the
576 SARS-CoV-2 infection site. In contrast, MK-8722, as systemic drug, may reach these tissues with minimal
577 side effects, as a daily treatment in diabetic Non-human primates (NHPs) with MK-8722 (10 mg/kg) for a
578 month induced only a limited and reversible cardiac hypertrophy [36]. The MK-8722 antiviral treatment we
579 report is efficient *in vitro* not only when applied from the onset of infection but also after infection.
580 Therefore, MK-8722 might be tested as post-exposure prophylaxis against SARS-CoV-2, thereby limiting
581 potential severe outcomes.

582

583 Mechanistically, we demonstrated here that AMPK activation by MK-8722 reduces lipid synthesis
584 through the inhibition of ACC by acting on the limiting step of fatty acid production and, consequently,
585 of phospholipid synthesis. This inhibition leads to a reduction in the formation of lipid droplets and a
586 significant reduction in the infectivity of viral particles. Lipid synthesis is required to extend endoplasmic
587 reticulum for the genesis of the viral factories and to generate the viral membrane of SARS-CoV-2, which
588 is an enveloped virus. Changes in lipid content of viral particles have been shown to impact infectivity
589 [5,7,9,11]. AMPK-mediated inhibition of ACC by MK-8722 treatment likely modifies all membrane lipid

590 species in SARS-CoV-2 infected cells [56], in turn affecting viral membrane lipid composition and likely the
591 lower virus infectivity we observed. The modification of the cellular lipid content by MK-8722 treatment
592 might also block the release of pro-inflammatory molecules otherwise induced by infection, such as IL-6
593 and LTB4 [12,57]. SARS-CoV-2 affects also cholesterol metabolism [7,58,59] and patients under statins who
594 contracted SARS-CoV-2 developed better T cell responses and showed lower grade of pulmonary
595 symptoms [60,61]. AMPK activation also inhibits HMG-CoA-reductase, the major enzyme for cholesterol
596 synthesis. MK-8722 treatment might therefore be beneficial for COVID-19 patients through multiple
597 mechanisms [7,14,17]. The molecular mechanisms underlying the changes in the lipid spectrum and
598 cholesterol content in infected cells following treatment with MK-8722 remain to be understood.

599 Increased activation of ULK1 and expression of Sequestosome-1/p62 upon MK-8722 treatment *in vitro*
600 reflects a restoration of the autophagy flux and the targeting of viruses to lysosome for degradation.
601 This mechanism is otherwise blocked by viral replication in an ORF3- and ORF7a-mediated process,
602 which inhibits HOPS complex-mediated assembly of the SNARE complex required for autolysosome
603 formation [22,24,25]. Sequestrosome-1/p62 is an autophagy cargo receptor that plays a key role in
604 mediating the formation of autophagosomes and autophagic clearance of intracellular protein
605 aggregates by its binding to LC3b. A modification of p62 expression and LC3b binding capacity upon
606 SARS-CoV-2 infection has been observed *in vitro* [20,22,25]. Together, these data suggest that SARS-CoV-2-
607 mediated disruption of p62 expression and/or function impairs fusion of phagosome with lysosome
608 [20,22,62,63]. The increased p62 expression we observed upon MK-8722 treatment together with the
609 increased ULK1 activation will likely result in p62 activation, in turn promoting phagolysosomes
610 formation as we reported**.** Convergence of Beclin-Atg14 together with P62 activation could stimulated
611 the selective clearance of viral components, in a process called virophagy [64–66]. We thus propose that
612 AMPK pharmacological activation induces virophagy and is responsible, at least partially, for its antiviral

613 effect**.** Furthermore P62 also induces proteasomal degradation[67], and its increased expression could
614 contribute in the antiviral activity of MK-8722.

615 The restoration of autophagy by MK-8722 we report, and thereby degradation of viral components, will
616 improve MHC-I presentation and the cellular cytotoxic response [68], contributing to the therapeutic value
617 of MK-8722 treatment. Furthermore, defective viral particles, which are produced upon MK-8722
618 treatment, might be detected by innate immune sensors such as MAVS [69], promoting a type-I IFN
619 response and protection from SARS-CoV-2 infection [28]. MK-8722 treatment of infected cells also unlocks
620 the IFN-I response, as shown by the increase in *IFNα* and both ISG *Mx1* and *OAS1* mRNA we observed.
621 This IFN-I response most likely associates with a better control of infection and lowers pathology score
622 [26,27,29,41,70]. The induction of IFNβ by poly I:C is only transient, with its mRNA returning even to a level
623 below the basal one [71]. Here, continuous but not post infection treatment with MK-8722 may similarly
624 result in a transient accumulation of *IFNβ* mRNA, the final level of which is statistically lower than that
625 observed in the absence of treatment. This faster IFN-I response could enhance protection of individuals
626 against SARS-CoV-2, since a delay in IFN-I response is associated with disease severity [29,41] and post
627 infection treatment of severe COVID with IFNα2b significantly improved patient outcome [42].

628 Finally, MK-8722 could also enhance the response of SARS-CoV-2-specific $CD8^+$ T cells at the site of
629 infection which is crucial for protection in NHP and in humans [44–46]. Optimal $CD8^+$ T cells responses at
630 mucosal level can be boosted by IFN-I, which showed vaccine adjuvant-like properties in strategies
631 against other infectious diseases and cancer [72–75]. MK-8722 treatment, which stimulates the IFN-I
632 pathway upon infection, as shown here, could therefore contribute to improve the $CD8^+$ T cells
633 response. Accordingly, *in vitro*, MK-8722 does not antagonise but rather slightly enhance the T cell
634 response and when combined with $CD8^+$ T cells, resulting treatment increases inhibition of infection
635 compared to either treatment alone. Further studies on the crosstalk between $CD8^+$ T cells, phagocyte

636 and infected epithelial cells will clarify how MK-8722 modulates the $CD8^+$ T cell response. The antiviral
637 effect of AMPK activation in primary lung reconstruction and preclinical models such as hamster remains
638 to be tested.

639 In summary, to optimize safely antiviral treatment against SARS-CoV-2, as summarized in the graphical
640 abstract, we propose here to target the energy sensor AMPK using small molecule pan-AMPK allosteric
641 activators (such as MK-8722), rather than targeting the virus itself. The antiviral mechanism of MK-8722
642 relies on the reversion of three major pathways affected by SARS-CoV-2 infection, namely lipid
643 metabolism, autophagy and IFN-I response. Therefore, to escape MK-8722 and generate resistant and
644 more pathogenic variants, SARS-CoV-2 will need to acquire a higher number of resistance mutations
645 than a drug targeting on a single pathway. Furthermore, by increasing the SARS-CoV-2 $CD8^+$ T cell
646 response, MK-8722 treatment would result in a faster response against infection and better outcome.
647 *Coronaviruses* but also *Flaviviruses* replicate within viral factories and/or disturb lipid metabolism, hijack
648 autophagy and IFN-I response. We therefore propose that MK-8722 could act as antiviral against other
649 *Coronaviruses* and *Flaviviruses*, ensuring a larger available therapeutic arsenal against future emerging
650 virosis.

651

652 **References**

653

654 1. Fernandes, Q. *et al.* Emerging COVID-19 variants and their impact on SARS-CoV-2 diagnosis,
655 therapeutics and vaccines. *Ann Med* **54**, 524–540 (2022).
656 2. Haque, Ashwaq, O., Sarief, A. & Azad John Mohamed, A. K. A comprehensive review about SARS-
657 CoV-2. *Future Virol* **15**, 625–648 (2020).
658 3. Ji, M. *et al.* VMP1 and TMEM41B are essential for DMV formation during β-coronavirus
659 infection. *J Cell Biol* **221**, e202112081 (2022).
660 4. Snijder, E. J. *et al.* A unifying structural and functional model of the coronavirus replication
661 organelle: Tracking down RNA synthesis. *PLOS Biology* **18**, e3000715 (2020).
662 5. Farley, S. E. *et al.* A global lipid map reveals host dependency factors conserved across SARS-
663 CoV-2 variants. *Nat Commun* **13**, 3487 (2022).
664 6. Tabata, K. *et al.* Convergent use of phosphatidic acid for hepatitis C virus and SARS-CoV-2

665 replication organelle formation. *Nat Commun* **12**, 7276 (2021).
666 7. Tanner, J. E. & Alfieri, C. The Fatty Acid Lipid Metabolism Nexus in COVID-19. *Viruses* **13**, 90
667 (2021).
668 8. Bajimaya, S., Frankl, T., Hayashi, T. & Takimoto, T. Cholesterol is required for stability and
669 infectivity of influenza A and respiratory syncytial viruses. *Virology* **510**, 234–241 (2017).
670 9. Cheng, N. *et al.* Protein post-translational modification in SARS-CoV-2 and host interaction. *Front*
671 *Immunol* **13**, 1068449 (2022).
672 10. McBride, C. E. & Machamer, C. E. Palmitoylation of SARS-CoV S protein is necessary for
673 partitioning into detergent-resistant membranes and cell–cell fusion but not interaction with M protein.
674 *Virology* **405**, 139–148 (2010).
675 11. Mesquita, F. S. *et al.* S-acylation controls SARS-CoV-2 membrane lipid organization and enhances
676 infectivity. *Dev Cell* **56**, 2790-2807.e8 (2021).
677 12. Dias, S. S. G. *et al.* Lipid droplets fuel SARS-CoV-2 replication and production of inflammatory
678 mediators. *PLoS Pathog* **16**, e1009127 (2020).
679 13. Grootemaat, A. E. *et al.* Lipid and Nucleocapsid N-Protein Accumulation in COVID-19 Patient
680 Lung and Infected Cells. *Microbiology Spectrum* **10**, e01271-21 (2022).
681 14. Nardacci, R. *et al.* Evidences for lipid involvement in SARS-CoV-2 cytopathogenesis. *Cell Death*
682 *Dis* **12**, 1–12 (2021).
683 15. Wang, W. *et al.* Genetic variety of ORF3a shapes SARS-CoV-2 fitness through modulation of lipid
684 droplet. *J Med Virol* **95**, e28630 (2023).
685 16. Chu, J. *et al.* Pharmacological inhibition of fatty acid synthesis blocks SARS-CoV-2 replication.
686 *Nat Metab* **3**, 1466–1475 (2021).
687 17. Koepke, L., Hirschenberger, M., Hayn, M., Kirchhoff, F. & Sparrer, K. M. Manipulation of
688 autophagy by SARS-CoV-2 proteins. *Autophagy* **17**, 2659–2661 (2021).
689 18. Gassen, N. C. *et al.* SARS-CoV-2-mediated dysregulation of metabolism and autophagy uncovers
690 host-targeting antivirals. *Nat Commun* **12**, 3818 (2021).
691 19. Zhou, H., Hu, Z. & Castro-Gonzalez, S. Bidirectional interplay between SARS-CoV-2 and
692 autophagy. *mBio* **0**, e01020-23 (2023).
693 20. Zhang, Y., Liu, S., Xu, Q., Li, H. & Lu, K. Cleavage of the selective autophagy receptor
694 SQSTM1/p62 by the SARS-CoV-2 main protease NSP5 prevents the autophagic degradation of viral
695 membrane proteins. *Mol Biomed* **3**, 17 (2022).
696 21. Twu, W.-I. *et al.* Contribution of autophagy machinery factors to HCV and SARS-CoV-2
697 replication organelle formation. *Cell Rep* **37**, 110049 (2021).
698 22. Hou, P. *et al.* The ORF7a protein of SARS-CoV-2 initiates autophagy and limits autophagosome-
699 lysosome fusion via degradation of SNAP29 to promote virus replication. *Autophagy* **19**, 551–569 (2023).
700 23. Koyama-Honda, I., Itakura, E., Fujiwara, T. K. & Mizushima, N. Temporal analysis of recruitment
701 of mammalian ATG proteins to the autophagosome formation site. *Autophagy* **9**, 1491–1499 (2013).
702 24. Miao, G. *et al.* ORF3a of the COVID-19 virus SARS-CoV-2 blocks HOPS complex-mediated
703 assembly of the SNARE complex required for autolysosome formation. *Dev Cell* **56**, 427-442.e5 (2021).
704 25. Zhang *et al.* The SARS-CoV-2 protein ORF3a inhibits fusion of autophagosomes with lysosomes.
705 *Cell Discov* **7**, 31 (2021).
706 26. Bizzotto, J. *et al.* SARS-CoV-2 Infection Boosts MX1 Antiviral Effector in COVID-19 Patients.
707 *iScience* **23**, 101585 (2020).
708 27. Danziger, O., Patel, R. S., DeGrace, E. J., Rosen, M. R. & Rosenberg, B. R. Inducible CRISPR
709 activation screen for interferon-stimulated genes identifies OAS1 as a SARS-CoV-2 restriction factor.
710 *PLOS Pathogens* **18**, e1010464 (2022).
711 28. Li, X. *et al.* SARS-CoV-2 ORF10 suppresses the antiviral innate immune response by degrading
712 MAVS through mitophagy. *Cell Mol Immunol* **19**, 67–78 (2022).

713 29. Smith, N. *et al.* Defective activation and regulation of type I interferon immunity is associated
714 with increasing COVID-19 severity. *Nat Commun* **13**, 7254 (2022).
715 30. Øynebråten, I. Involvement of autophagy in MHC class I antigen presentation. *Scand J Immunol*
716 **92**, e12978 (2020).
717 31. Wen, Z. *et al.* Enhancement of SARS-CoV-2 N Antigen-Specific T Cell Functionality by Modulating
718 the Autophagy-Mediated Signal Pathway in Mice. *Viruses* **15**, 1316 (2023).
719 32. Zhang *et al.* The ORF8 protein of SARS-CoV-2 mediates immune evasion through down-
720 regulating MHC-I. *Proc Natl Acad Sci U S A* **118**, e2024202118 (2021).
721 33. Steinberg, G. R. & Hardie, D. G. New insights into activation and function of the AMPK. *Nat Rev*
722 *Mol Cell Biol* **24**, 255–272 (2023).
723 34. Moreira, D. *et al.* AMP-activated protein kinase as a target for pathogens: friends or foes? *Curr*
724 *Drug Targets* **17**, 942–953 (2016).
725 35. Farfan-Morales, C. N. *et al.* The antiviral effect of metformin on zika and dengue virus infection.
726 *Sci Rep* **11**, 8743 (2021).
727 36. Myers, R. W. *et al.* Systemic pan-AMPK activator MK-8722 improves glucose homeostasis but
728 induces cardiac hypertrophy. *Science* **357**, 507–511 (2017).
729 37. Muise, E. S. *et al.* Pharmacological AMPK activation induces transcriptional responses congruent
730 to exercise in skeletal and cardiac muscle, adipose tissues and liver. *PLOS ONE* **14**, e0211568 (2019).
731 38. Cottignies-Calamarte, A., He, F., Zhu, A., Real, F. & Bomsel, M. Protocol to detect infectious
732 SARS-CoV-2 at low levels using in situ hybridization techniques. *STAR Protocols* **4**, 102593 (2023).
733 39. Desmarets, L. *et al.* A reporter cell line for the automated quantification of SARS-CoV-2 infection
734 in living cells. *Front Microbiol* **13**, 1031204 (2022).
735 40. Lu, X. *et al.* US CDC Real-Time Reverse Transcription PCR Panel for Detection of Severe Acute
736 Respiratory Syndrome Coronavirus 2. *Emerg Infect Dis* **26**, 1654–1665 (2020).
737 41. Decker, T. The early interferon catches the SARS-CoV-2. *Journal of Experimental Medicine* **218**,
738 e20211667 (2021).
739 42. Zhou, Q. *et al.* Interferon-α2b Treatment for COVID-19. *Front Immunol* **11**, 1061 (2020).
740 43. Schroeder, S. *et al.* Interferon antagonism by SARS-CoV-2: a functional study using reverse
741 genetics. *The Lancet Microbe* **2**, e210–e218 (2021).
742 44. Liu, J. *et al.* CD8 T cells contribute to vaccine protection against SARS-CoV-2 in macaques. *Sci*
743 *Immunol* **7**, eabq7647 (2022).
744 45. Taus, E. *et al.* Dominant CD8+ T Cell Nucleocapsid Targeting in SARS-CoV-2 Infection and Broad
745 Spike Targeting From Vaccination. *Front Immunol* **13**, 835830 (2022).
746 46. Vitiello, L. *et al.* Long Lasting Cellular Immune Response Induced by mRNA Vaccination:
747 Implication for Prevention Strategies. *Front Immunol* **13**, 836495 (2022).
748 47. Parthasarathy, H., Tandel, D., Siddiqui, A. H. & Harshan, K. H. Metformin suppresses SARS-CoV-2
749 in cell culture. *Virus Research* **323**, 199010 (2023).
750 48. Bonnet, R., Mariault, L. & Peyron, J.-F. Identification of potentially anti-COVID-19 active drugs
751 using the connectivity MAP. *PLoS One* **17**, e0262751 (2022).
752 49. Doshi, H. *et al.* AMPK protects endothelial cells against HSV-1 replication via inhibition of
753 mTORC1 and ACC1. *Microbiol Spectr* **11**, e0041723 (2023).
754 50. Farfan-Morales, C. N. *et al.* Anti-flavivirus Properties of Lipid-Lowering Drugs. *Frontiers in*
755 *Physiology* **12**, (2021).
756 51. Jiménez de Oya, N., Blázquez, A.-B., Casas, J., Saiz, J.-C. & Martín-Acebes, M. A. Direct Activation
757 of Adenosine Monophosphate-Activated Protein Kinase (AMPK) by PF-06409577 Inhibits Flavivirus
758 Infection through Modification of Host Cell Lipid Metabolism. *Antimicrob Agents Chemother* **62**, e00360-
759 18 (2018).
760 52. Prasad, V. *et al.* Enhanced SARS-CoV-2 entry via UPR-dependent AMPK-related kinase NUAK2.

761 *Molecular Cell* **83**, 2559-2577.e8 (2023).
762 53. Yuan, W.-C. *et al.* NUAK2 is a critical YAP target in liver cancer. *Nat Commun* **9**, 4834 (2018).
763 54. Erickson, S. M. *et al.* Metformin for Treatment of Acute COVID-19: Systematic Review of Clinical
764 Trial Data Against SARS-CoV-2. *Diabetes Care* **46**, 1432–1442 (2023).
765 55. Foretz, M., Even, P. C. & Viollet, B. AMPK Activation Reduces Hepatic Lipid Content by Increasing
766 Fat Oxidation In Vivo. *Int J Mol Sci* **19**, E2826 (2018).
767 56. Yeudall, S. *et al.* Macrophage acetyl-CoA carboxylase regulates acute inflammation through
768 control of glucose and lipid metabolism. *Sci Adv* **8**, eabq1984 (2022).
769 57. Fomin, G. *et al.* Cytokine response and damages in the lungs of aging Syrian hamsters on a high-
770 fat diet infected with the SARS-CoV-2 virus. *Front Immunol* **14**, 1223086 (2023).
771 58. Tsai, P.-H. *et al.* Modifications of lipid pathways restrict SARS-CoV-2 propagation in human
772 induced pluripotent stem cell-derived 3D airway organoids. *Journal of Advanced Research* (2023)
773 doi:10.1016/j.jare.2023.08.005.
774 59. Yuan, Y. *et al.* The CH24H metabolite, 24HC, blocks viral entry by disrupting intracellular
775 cholesterol homeostasis. *Redox Biol* **64**, 102769 (2023).
776 60. Santosa, A. *et al.* Protective effects of statins on COVID-19 risk, severity and fatal outcome: a
777 nationwide Swedish cohort study. *Sci Rep* **12**, 12047 (2022).
778 61. Teixeira, L. *et al.* Simvastatin Downregulates the SARS-CoV-2-Induced Inflammatory Response
779 and Impairs Viral Infection Through Disruption of Lipid Rafts. *Front Immunol* **13**, 820131 (2022).
780 62. Paunovic, V. *et al.* Autophagy Receptor p62 Regulates SARS-CoV-2-Induced Inflammation in
781 COVID-19. *Cells* **12**, 1282 (2023).
782 63. Tan, X. *et al.* Coronavirus subverts ER-phagy by hijacking FAM134B and ATL3 into p62
783 condensates to facilitate viral replication. *Cell Rep* **42**, 112286 (2023).
784 64. Thinwa, J. W. *et al.* CDKL5 regulates p62-mediated selective autophagy and confers protection
785 against neurotropic viruses. *J Clin Invest* **134**, e168544 (2024).
786 65. Dong, X. *et al.* Sorting nexin 5 mediates virus-induced autophagy and immunity. *Nature* **589**,
787 456–461 (2021).
788 66. Gassen, N. C. *et al.* SKP2 attenuates autophagy through Beclin1-ubiquitination and its inhibition
789 reduces MERS-Coronavirus infection. *Nat Commun* **10**, 5770 (2019).
790 67. Kumar, A. V., Mills, J. & Lapierre, L. R. Selective Autophagy Receptor p62/SQSTM1, a Pivotal
791 Player in Stress and Aging. *Frontiers in Cell and Developmental Biology* **10**, (2022).
792 68. Gestal-Mato, U. & Herhaus, L. Autophagy-dependent regulation of MHC-I molecule
793 presentation. *J Cell Biochem* (2023) doi:10.1002/jcb.30416.
794 69. Manzoni, T. B. & López, C. B. Defective (interfering) viral genomes re-explored: impact on
795 antiviral immunity and virus persistence. *Future Virol* **13**, 493–503 (2018).
796 70. Yang, E. & Li, M. M. H. All About the RNA: Interferon-Stimulated Genes That Interfere With Viral
797 RNA Processes. *Front Immunol* **11**, 605024 (2020).
798 71. Abe, K. *et al.* Analysis of interferon-beta mRNA stability control after poly(I:C) stimulation using
799 RNA metabolic labeling by ethynyluridine. *Biochem Biophys Res Commun* **428**, 44–49 (2012).
800 72. Cabral-Piccin, M. P. *et al.* Primary role of type I interferons for the induction of functionally
801 optimal antigen-specific CD8+ T cells in HIV infection. *EBioMedicine* **91**, 104557 (2023).
802 73. Hemann, E. A. *et al.* A Small Molecule RIG-I Agonist Serves as an Adjuvant to Induce Broad
803 Multifaceted Influenza Virus Vaccine Immunity. *J Immunol* **210**, 1247–1256 (2023).
804 74. Proietti, E. *et al.* Type I IFN as a Natural Adjuvant for a Protective Immune Response: Lessons
805 from the Influenza Vaccine Model1. *The Journal of Immunology* **169**, 375–383 (2002).
806 75. Sasaki, E. *et al.* Systemically inoculated adjuvants stimulate pDC-dependent IgA response in local
807 site. *Mucosal Immunol* **16**, 275–286 (2023).
808

809 **Figure Legends**

810

811 **Figure 1: MK-8722 inhibits SARS-CoV-2 replication *in vitro.***

812 **A:** ***Schematic outline of the continuous treatment protocol with MK-8722***.

813 **B-D:** ***Dose dependent inhibition of Vero76 and Calu-3 cell infection with SARS-CoV2 by continuous***
814 ***treatment with MK-8722***. Inhibition of infection with indicated SARS-CoV-2 variant in Vero76 was
815 measured by flow cytometry (**B**) and that of Calu-3 by FISH-flow (**C-D**). n≥5 independent experiments.
816 Labelling for SARS-CoV-2 Spike (Black) and for viral RNA (Red).

817 **E:** ***Dose-dependent inhibition of viral genome release from Calu-3 cells*** infected with the Alpha variant
818 after continuous treatment with MK-8722 measured by quantification of *N* RNA in the supernatant by
819 RT-qPCR. n≥5 independent experiments.

820 **F-G:** ***Inhibition of viral replication after MK-8722 treatment.*** Cells were incubated with the indicated
821 SARS-CoV-2 variant in the absence or the presence of the drug (1 µM for Vero76 **(F)** and 5µM for Calu-3
822 cells **(G)**) for 1h at 4°C to synchronize infection and chased for 1h or for an additional 24h in the case of
823 Vero76 cells and for 32h in the case of Calu-3 cells at 37°C. *N* RNA was quantified in cellular extracts by
824 RT-qPCR. n≥5 independent experiments.

825 **H**: ***Schematic representation of the post-exposure treatment protocol with MK-8722.***

826 **I-J**: ***Post-exposure treatment with MK-8722 is sufficient to block infection by SARS-CoV-2.*** Cells were
827 left untreated or treated with MK-8722 (5 µM) either continuously with Alpha variant or treated post-
828 infection as in **G**. Infection was evaluated by quantification of Spike expression by flow cytometry (**I**) or
829 by RT-qPCR using the $2^{-\Delta\Delta Ct}$ method (**J**). Values represent infection inhibition. n≥6 independent
830 experiments. Shown are mean ± SEM.

831 ANOVA: * $p<0.05$, ** $p<0.01$, *** $p<0.001$, **** $p<0.0001$.

832

833 **Figure 2: MK-8722-dependent AMPK activation inhibits SARS-CoV-2 replication by inhibition of the**
834 **lipid biosynthetic pathway and restoration of the autophagy flux.**

835 **A**: **Activation or expression ratio of AMPK, ACC, raptor, ULK1, p62 and Nucleocapsid were analyzed by**
836 **western blot** in Vero76 and Calu-3 cells after continuous MK-8722 treatment as indicated in Figure 1A
837 Western blots were quantified by ImageJ, and each marker value in indicated condition was normalized
838 over corresponding marker expression value in the non-infected non-treated condition. Shown are
839 mean ± SEM. n≥2 independent experiments.

840 **B: *Quantification of the western blot presented as Heat maps:*** Heat maps represent the transformation
841 by Log2 of the expression/phosphorylation values quantified on each blot by ImageJ relative to
842 corresponding non-infected non-treated condition for Vero76 and Calu-3 cells. n≥2 independent
843 experiments. Student's *t*–test: * $p<0.05$, ** $p<0.01$.

844

845 **Figure 3: MK-8722 inhibition of SARS-CoV-2 is associated to decrease of lipid droplets and release of**
846 **defective viral particles.**
847 **A: *Morphological analyses.*** Calu-3 cells were infected with the SARS-CoV-2 Alpha variant in the
848 presence of a continuous treatment with MK-8722 (5 µM) or not. At 3dpi, lipids droplets, defined as
849 indicated in the method section, were stained with Nile Red lipophilic dye before cells fixation.
850 Nucleoprotein protein (Green) expression detected by immunofluorescence, Nile Red (Red) staining and
851 nuclei staining with DAPI (Blue) were observed by confocal microscopy. One representative field out of 5
852 observed per condition are presented. Bar: 20 µm. Shown are images representative of n=3
853 independent experiments.
854 **B: *Quantitative analysis of images*** shown in A using ImageJ of the number, area and intensity of lipid
855 droplets (LD), as defined in the method section within infected cells, characterized by the expression of
856 Nucleocapsid protein. Values were normalized to corresponding infected non-treated condition. n=3
857 independent experiments.
858 **C: *Lipid droplets and N-protein colocalization*.** The fraction of lipid droplets colocalizing in Nucleocapsid
859 staining and inversely were quantified using JACoP plugin from ImageJ software and corresponding
860 Manders' overlap coefficients (MOC) are presented.
861 **D**: ***Viral genomes released***. Cells were infected with the Alpha SARS-CoV-2 variant in the absence or in
862 the presence of a continuously treatment with MK-8722 at the indicated concentrations. Viral *N* RNA
863 released by Vero76 cells at 1dpi (upper panel) and Calu-3 cells at 4dpi (lower panel) cells were
864 quantified by RT-qPCR. n≥3 independent experiments.
865 **E: *Viral titres released*** by Vero76 (upper panel) and Calu-3 (lower panel) cells treated as above in (**D**).
866 n=3 independent experiments.
867 **F: *Infectious index of released viruses*** determined as described in the methods section using matched
868 viral titres and viral copy number values Vero76 (upper panel) and Calu-3 (lower panel) cells obtained as
869 in (**D**) and (**E**). n=4 independent experiments.
870

871 Student's *t*–test and Mann-Whitney * $p<0.05$, ** $p<0.01$, *** $p<0.001$, **** $p<0.0001$.

872

873 **Figure 4: MK-8722 treatment increases the autophagic flux redirecting viral components to**
874 **lysosomes and restores type I interferon responses."**

875 **A: *Morphological analysis***: Calu-3 cells were infected with the SARS-CoV-2 Alpha variant in the presence
876 of a continuously treatment with MK-8722 (5 µM) or not. At 3dpi, cells were then fixed and LAMP1 (Red)
877 and Nucleocapside N (Green) protein expression was detected by immunofluorescence. Nuclei were
878 stained with DAPI (Blue). Cells were observed by confocal microscopy. One representative field out of 5
879 observed per condition is presented. Bar: 20 µm. Images representative of n=3 independent
880 experiments.

881 **B: *Quantitative analysis*** of images show in A using ImageJ of number, area and intensity of lysosomes,
882 identified as defined in the methods section, within infected cells, characterized by the expression of
883 Nucleocapsid protein. Values were normalized to infected non-treated condition. n=3 independent
884 experiments.

885 **C: *LAMP1 and N protein colocalization*.** The fraction lysosomal objects colocalizing with Nucleocapsid
886 staining and inversely were quantified using JACoP plugin from ImageJ software and corresponding
887 Manders' overlap coefficients (MOC) are presented. n=3 independent experiments.

888 ***D: Morphological analysis**:* Calu-3 cells were infected with the SARS-CoV-2 Alpha variant in the presence
889 of a continuously treatment with MK-8722 (5 µM) or not. At 3dpi, cells were then fixed and LAMP1 (Red)
890 and LC3b (Green) protein expression was detected by immunofluorescence. Nuclei were stained with
891 DAPI (Blue). Cells were observed by confocal microscopy. One representative field out of 4 observed per
892 condition is presented. Bar: 20 µm. Images representative of n=3 independent experiments.

893 ***E: LAMP1 and LC3b protein colocalization*.** The fraction lysosomal objects colocalizing with LC3b foci
894 staining and inversely, were quantified using JACoP plugin from ImageJ software and corresponding
895 Manders' overlap coefficients (MOC) are presented. n=3 independent experiments.

896 ***F: Lysosomal activity.*** Calu-3 cells were infected with the indicated SARS-CoV-2 variant in the presence
897 of indicated MK-8722 concentration added at 24hpi and cultured for another 24h. Lysosomal activity
898 was then analysed using Lysotracker DND99 dye and quantified by flow cytometry. Shown are
899 lysotracker MFI collected from n≥5000 cells analysed. n=3 experiment.

900 ***G: IFN-I response***. Calu-3 cells were infected with SARS-CoV-2 Alpha variant in the presence of MK-8722
901 (5 µM) continuous treatment (dark orange) or initiated at 8hpi (light orange) or without treatment
902 (Blue). IFN-I response was evaluated by quantifying *IFNα*, *INFβ*, *Mx1* and *OAS1* mRNA by RT-qPCR of

903 indicated genes at 1dpi. Data represent the expression of each mRNA relative to *β-actin* mRNA levels,
904 and expressed following the $2^{-\Delta\Delta Ct}$ method. n=3 independent experiments.
905 ANOVA and Mann-Whitney * $p<0.05$, ** $p<0.01$, *** $p<0.001$, **** $p<0.0001$.
906
907 **Figure 5: MK-8722 treatment does not alter T cell response from vaccinated individuals against SARS-**
908 **CoV-2 *in vitro*.**
909 **A:** PBMCs from healthy SARS-CoV-2 vaccinated donors depleted in CD14 cells were stimulated for 6h
910 with anti-CD3 and anti-CD28 antibodies in the absence or in presence of MK-8722 (5 µM). IFNγ^+ and
911 CD107a$^+$ cell frequencies within CD4$^+$ and CD8$^+$ T cell populations were evaluated by flow cytometry. n=5
912 independent donors analysed in independent experiments.
913 **B:** CD14-depleted PBMCs from corresponding donors in **(A)** were stimulated for 6h with a T cell SARS-
914 CoV-2 spike peptide pool (Peptivator, Miltenyi), IFNγ^+ and CD107a$^+$ cell frequencies were quantified as in
915 (A). Activation levels are presented as activation index calculated as described in the methods section.
916 n≥3 independent donors analysed in independent experiments.
917 **C:** Caco2 cells were infected 2h with the Alpha variant of SARS-CoV-2 and treated post exposure (8hpi)
918 with MK-8722 (5 µM) alone or together with CD8$^+$ T cells from SARS-CoV-2 vaccinated individuals.
919 Infection was evaluated by quantification of Spike expression in cells at 2dpi by flow cytometry and
920 presented as inhibition of Spike expression frequency. n=5 independent donors performed in
921 independent experiments. Data presented are mean ± SEM.
922
923 ANOVA and *t*-test: * $p<0.05$, ** $p<0.01$, *** $p<0.001$, **** $p<0.0001$
924
925 **Supplementary Figure Legends**
926 ***Supplementary Figure S1: Kinetic of AMPK activation and downstream ACC phosphorylation*** evaluated
927 by western-blot after MK-8722 stimulation of Vero76.
928
929 ***Supplementary Figure S2: MK-8722 inhibits SARS-CoV-2 infection.***
930 **A:** Gating strategies used to analyse infection inhibition by MK-7822 treatment in Vero76 cells in Figure
931 1B.

932 **B:** Cells were treated as indicated in Figure 1B. Frequencies of infection in corresponding experimental
933 sample shown in Figure 1B were measured by SARS-CoV-2 Spike detection in Vero76 cells. Shown are
934 mean ± SEM. n=4 independent experiments.
935 **C:** Gating strategies used to analyse infection inhibition by MK-7822 treatment in Calu-3 cells in Figure
936 1C.
937 **D-E:** Cells were treated as indicated in Figure 1B and C. Frequencies of infection in corresponding
938 experimental sample shown in Figure 1B and C were measured by dual detection of Spike (Black) and
939 viral RNA (Red) using Fish-flow in Calu-3 cells infected by Alpha **(D)** or Omicron **(E)** variant, quantified by
940 flow cytometry. Shown are mean ± SEM. n=4 independent experiments.
941 **F**: Inhibition of infection by Remdesevir. Calu-3 cells were treated with Remdesivir (0.1 µM or 1 µM) 1h
942 prior and during the 2h of inoculation with SARS-CoV-2 Alpha variant. After virus removal, treatment
943 with Remdesivir at indicated concentration was continued. At 4dpi, infection was quantified by dual
944 detection of Spike (Black) and viral RNA (Red) in Fish-flow quantified by flow cytometry. Shown are
945 mean ± SEM of Spike and vRNA frequency (left) and infection inhibition (right). n=3 independent
946 experiments.
947 ***G-H***: ACE2 expression and viability were evaluated in Vero76 cells after 24h or in Calu-3 cells after 4days
948 of MK-8722 continuous treatment (1 µM or 5 µM respectively) by flow cytometry. ACE2 expression is
949 expressed as MFI (***G***) and viability as frequency of cells non-stained by the amine-reactive dye Viobility
950 (***H***). n=3 independent experiments.
951 ***I:*** Evaluation of MK-8722 over time and concentration in Calu-3 cells. n=3 independent experiments.
952 Shown are mean ± SEM. ANOVA: * $p<0.05$, ** $p<0.01$, *** $p<0.001$, **** $p<0.0001$.

953 **Supplementary Figure S3:** ***Evaluation of MK-8722 activity on cellular pathways downstream AMPK***
954 ***activation by western blot*** of ACC, ULK1, Raptor and AMPK phosphorylation, and Nucleocapsid protein
955 N and autophagy cargo receptor p62 expression in Vero76 **(A)** and Calu-3 cells **(B)** infected or not and
956 continuously treated or not with MK-8722 (5 µM) as indicated. The image shown is a montage of non-
957 adjacent from same western blots experiments used to evaluate each protein and, when indicated,
958 corresponding phosphorylated form.

959 ***Supplementary Figure S4: MK-8722 treatment decreases lipid droplet distribution in uninfected Calu-3***
960 ***cells.***

961 **A:** Cells were left uninfected and treated with MK-8722 (5 µM) or not and analyzed as indicated in Figure
962 3. Representative fields for Nile Red (Red) and Nucleocapsid N protein immunodetection (Green) imaged
963 by confocal microscopy are shown. Nuclei were stained with DAPI (Blue). Bars: 20 µm
964 **B:** Cells were treated and labelled as described in Figure 3. Total intensity of total Nile Red staining per
965 cell was calculated in ImageJ for non-infected non-treated (Ni-NT), infected non-treated (Infected-NT)
966 and Infected MK-8722 treated conditions. Values were normalized to the mean of non-infected non-
967 treated condition (Ni-NT). Shown are mean ± SEM. n= 3 independent experiments. ANOVA: $p<0.05$.
968
969 ***Supplementary Figure S5: MK-8722 impacts lysosomal parameters in Calu-3 cells.***
970 **A:** Cells were left uninfected but treated with MK-8722 (5 µM) or not and analysed as indicated in Figure
971 4. Representative fields for LAMP1 (Red) and Nucleocapsid N protein (Green) immunodetection imaged
972 by confocal microscopy are shown. Nuclei were stained with DAPI (Blue). Bars: 20 µm
973 **B:** Cells were treated and labelled as described in Figure 4. Total intensity of total LAMP1 staining per
974 cell was calculated in ImageJ for non-infected non-treated condition (Ni-NT), infected non-treated
975 (Infected-NT) and treated with 5 µM MK-8722 (Infected-MK-8722). Values were normalized to
976 corresponding non-infected non-treated condition. n≥3 independent experiments. Shown are mean ±
977 SEM. ANOVA: ** $p<0.01$ and *** $p<0.001$.
978
979 ***Supplementary Figure S6: Evaluation of nucleocapsid-specific T cell response in SARS-CoV-2 vaccinated***
980 ***individuals upon MK-8722 treatment ex vivo.***
981 **A:** PBMCs from healthy donors were cultivated for 6h indicated concentration of MK-8722 or
982 corresponding DMSO serving as carrier. CD4 and CD8 T cells activation (CD107a and IFNg expression)
983 was monitored by flow cytometry.
984 **B:** Gating strategy to investigate $CD4^+$ and $CD8^+$ T cell responses stimulation after activation with anti-
985 CD3/anti-CD28 antibodies (Transact) with or without MK-8722 treatment as analysed in Figure 5A.
986 **C:** CD14-depleted PBMCs corresponding to donors used in Figure 5 were stimulated as described in
987 Figure 5B but with T cell Nucleocapsid peptides (Peptivator, Miltenyi), and monitored by flow cytometry
988 for IFNγ and CD107a expression. Activation levels are presented as activation index as described in the
989 methods section. n≥3 independent donors.
990
991 ***Supplementary Figure S7: Gating strategy for combined MK-8722 treatment and $CD8^+$ T cell antiviral***
992 ***activity in coculture.***

993 Gating strategy to quantify the inhibition of Caco2 cells infection in the presence of MK-8722 and/or
994 $CD8^+$ T cells from vaccinated individuals shown in Figure 5C. Infection was evaluated within Caco2 cells
995 corresponding to the $CD3^-CD8^-$ population. The low number of $CD8^+$ T cells (around 150) prevented us
996 from investigating their activation level.

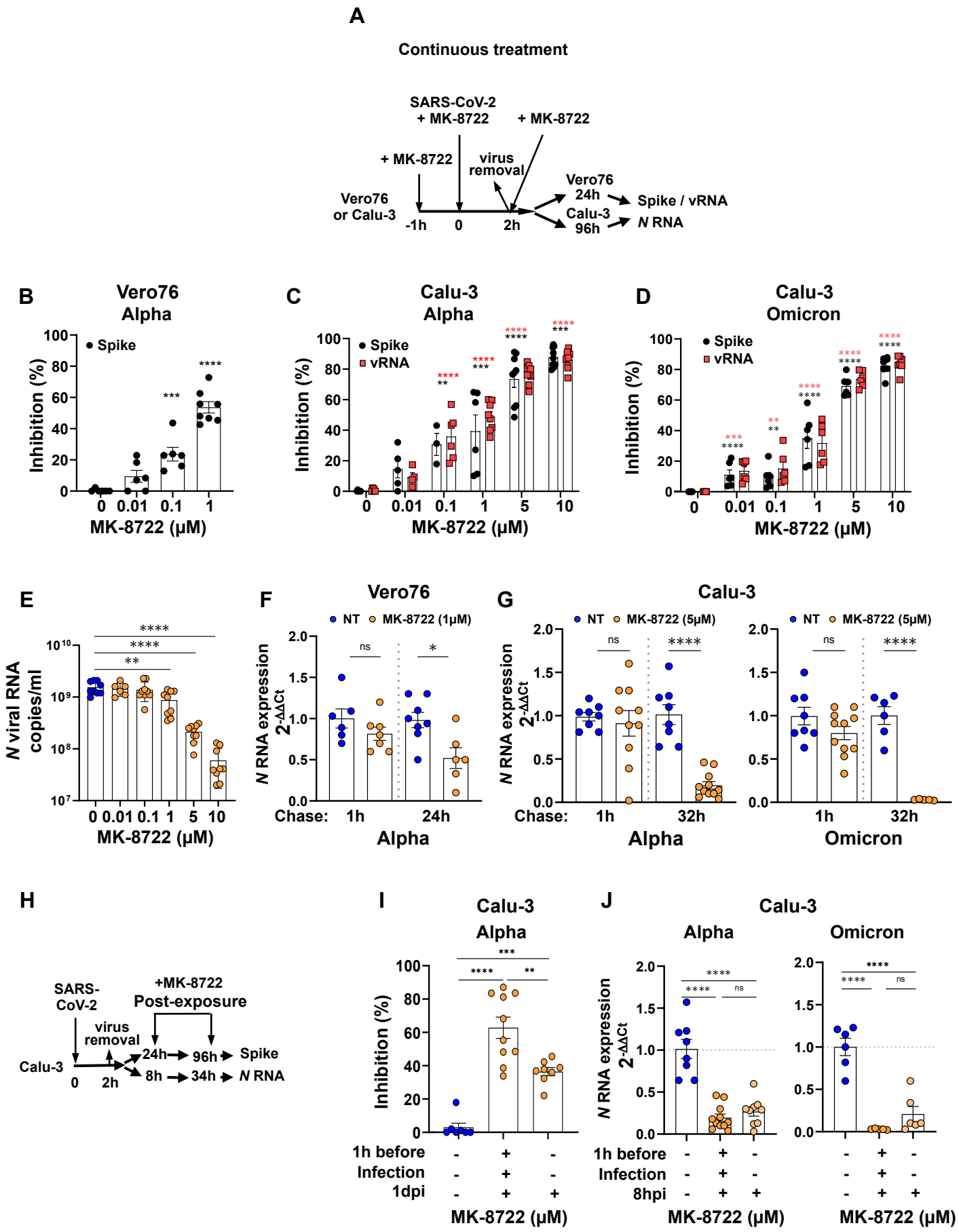
A
Continuous treatment
SARS-CoV-2
+ MK-8722
+ MK-8722
+ MK-8722
virus
removal
Vero76
or Calu-3
-1h
0
2h
Vero76
24h
Spike / vRNA
Calu-3
96h
N RNA
B
Vero76
Alpha
Spike
Inhibition (%)
MK-8722 (μM)
C
Calu-3
Alpha
Spike
vRNA
Inhibition (%)
MK-8722 (μM)
D
Calu-3
Omicron
Spike
vRNA
Inhibition (%)
MK-8722 (μM)
E
N viral RNA
copies/ml
MK-8722 (μM)
F
Vero76
NT
MK-8722 (1μM)
N RNA expression
2-ΔΔCt
Chase:
1h
24h
Alpha
G
Calu-3
NT
MK-8722 (5μM)
N RNA expression
2-ΔΔCt
Chase:
1h
32h
Alpha
Omicron
H
SARS-
CoV-2
+MK-8722
Post-exposure
virus
removal
Calu-3
0
2h
24h
96h
Spike
8h
34h
N RNA
I
Calu-3
Alpha
Inhibition (%)
1h before
Infection
1dpi
MK-8722 (μM)
J
Calu-3
Alpha
Omicron
N RNA expression
2-ΔΔCt
1h before
Infection
8hpi
MK-8722 (μM)
MK-8722 (μM)

Figure 1

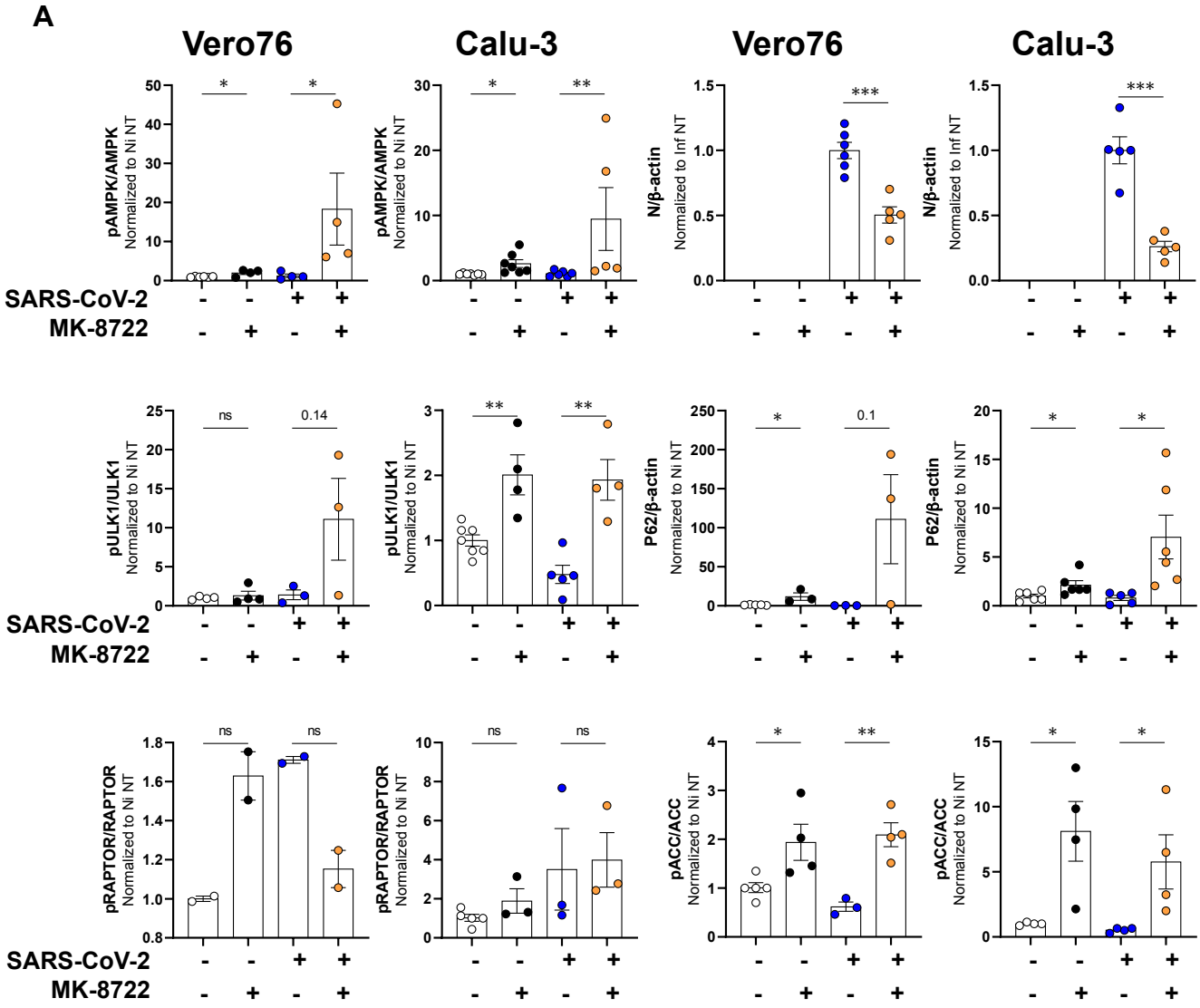
A
Vero76
Calu-3
Vero76
Calu-3
pAMPK/AMPK
Normalized to Ni NT
N/β-actin
Normalized to Inf NT
pULK1/ULK1
P62/β-actin
pRAPTOR/RAPTOR
pACC/ACC
SARS-CoV-2
MK-8722
ns
0.14
0.1

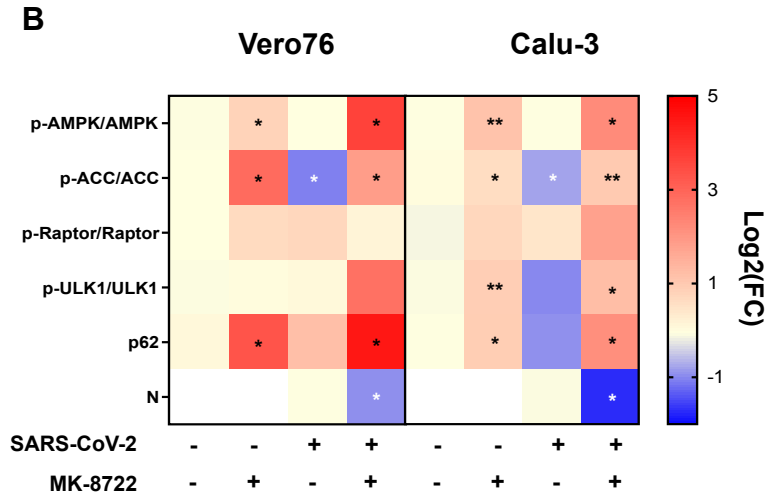
B
Vero76
Calu-3
p-AMPK/AMPK
p-ACC/ACC
p-Raptor/Raptor
p-ULK1/ULK1
p62
N
SARS-CoV-2
MK-8722
Log2(FC)

Figure 2

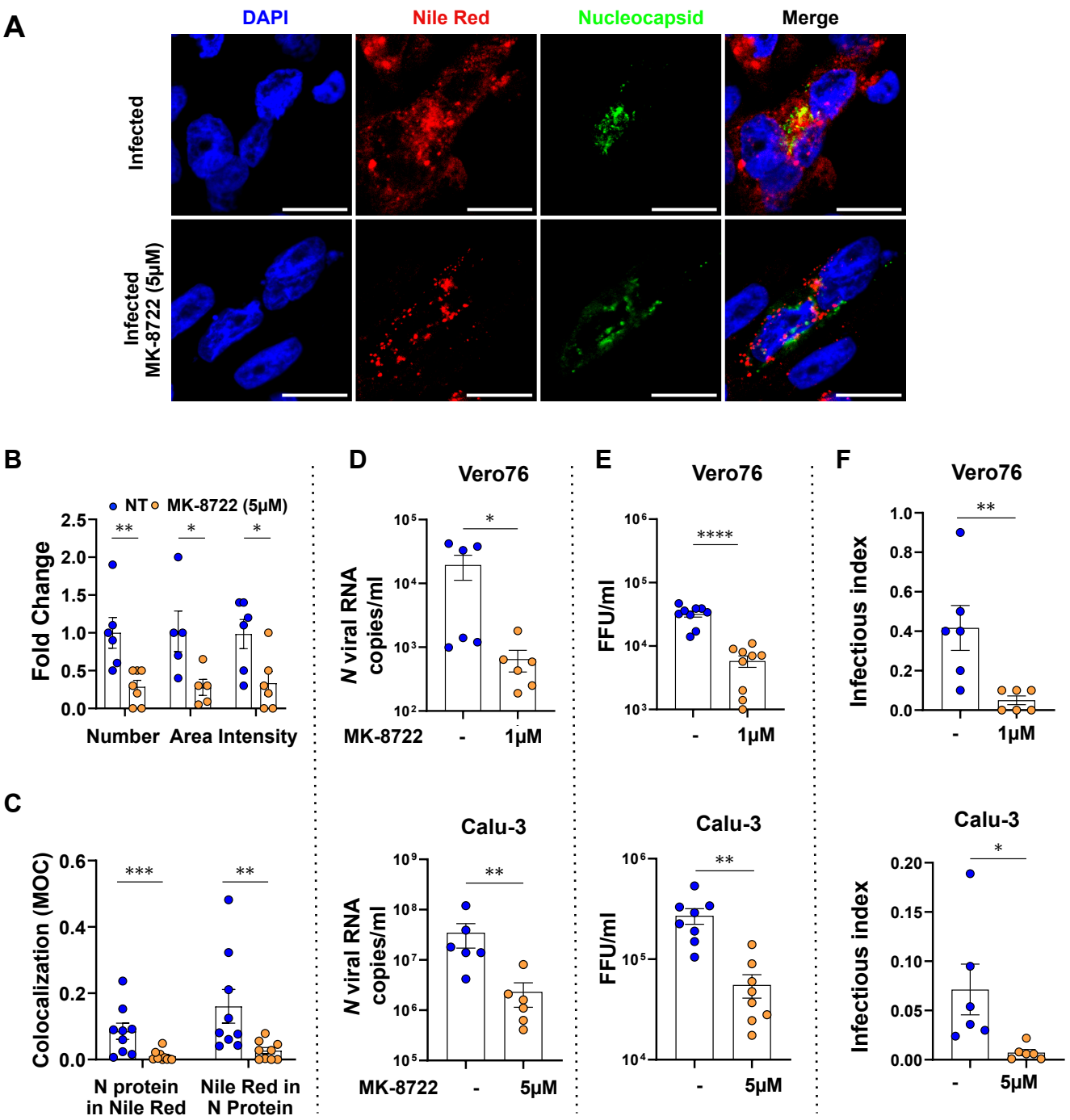
A
DAPI
Nile Red
Nucleocapsid
Merge
Infected
Infected MK-8722 (5μM)
B
NT
MK-8722 (5μM)
Fold Change
Number
Area
Intensity
C
Colocalization (MOC)
N protein in Nile Red
Nile Red in N Protein
D
Vero76
Calu-3
N viral RNA copies/ml
MK-8722
-
1μM
5μM
E
FFU/ml
F
Infectious index

Figure 3

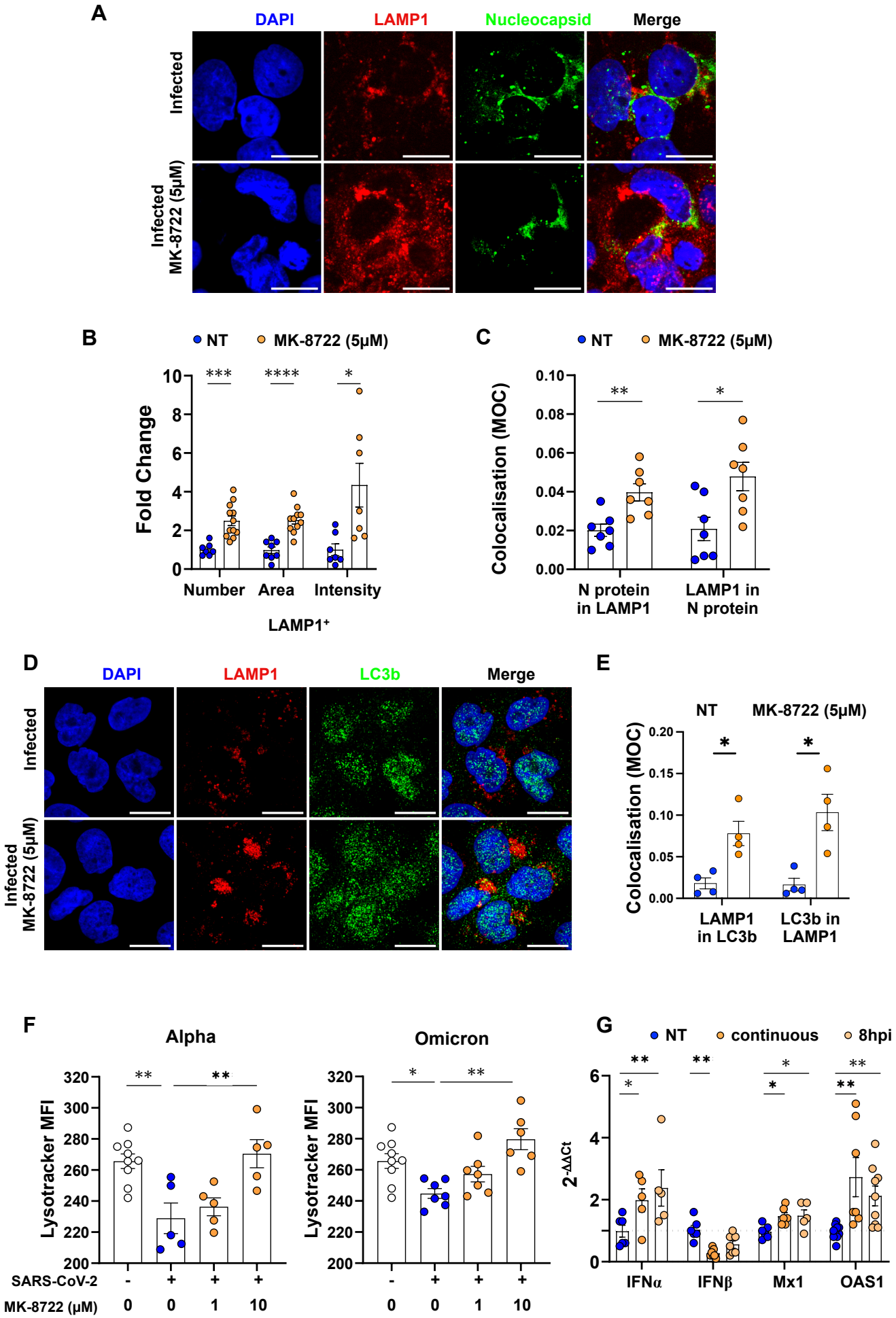
A
DAPI
LAMP1
Nucleocapsid
Merge
Infected
Infected MK-8722 (5μM)
B
NT
MK-8722 (5μM)
Fold Change
Number
Area
Intensity
LAMP1+
C
Colocalisation (MOC)
N protein in LAMP1
LAMP1 in N protein
D
LC3b
E
LAMP1 in LC3b
LC3b in LAMP1
F
Alpha
Omicron
Lysotracker MFI
SARS-CoV-2
MK-8722 (μM)
G
continuous
8hpi
2-ΔΔCt
IFNα
IFNβ
Mx1
OAS1

Figure 4

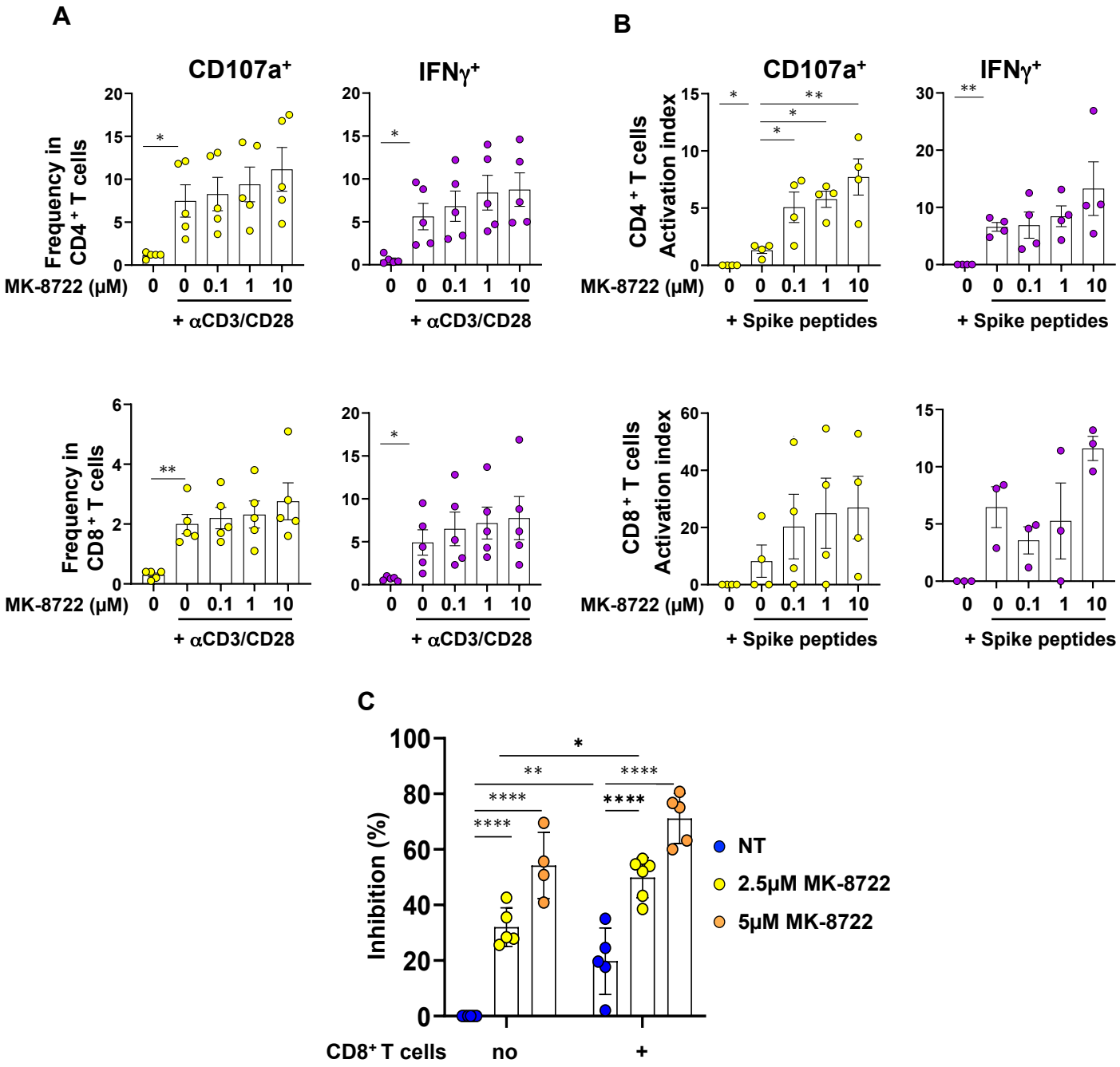
A
CD107a+
IFNγ+
Frequency in CD4+ T cells
MK-8722 (μM)
0 0 0.1 1 10
+ αCD3/CD28
B
CD4+ T cells Activation index
+ Spike peptides
Frequency in CD8+ T cells
CD8+ T cells Activation index
C
Inhibition (%)
NT
2.5μM MK-8722
5μM MK-8722
CD8+ T cells
no
+

Figure 5

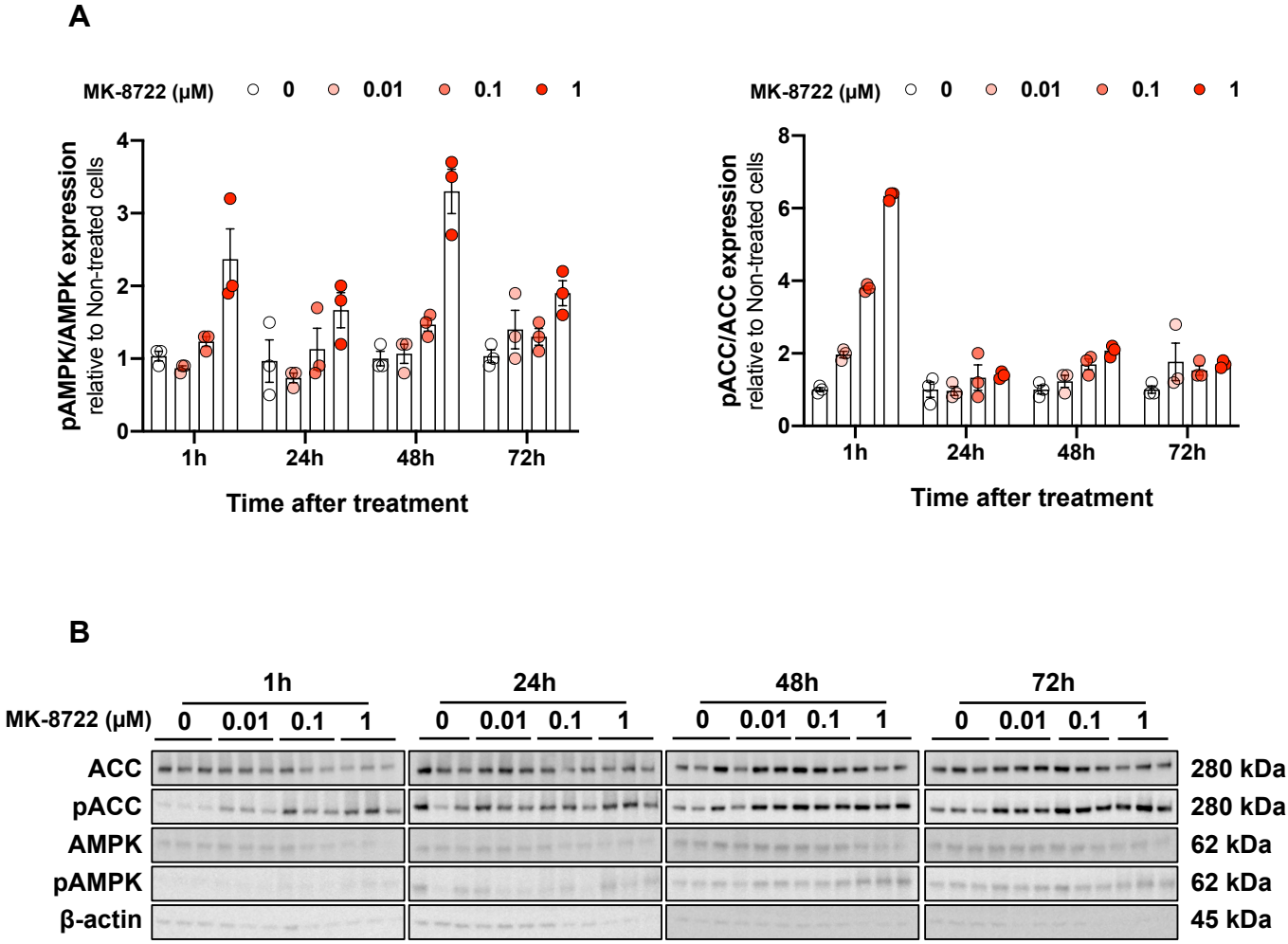
A
MK-8722 (μM)
0
0.01
0.1
1
pAMPK/AMPK expression
relative to Non-treated cells
1h
24h
48h
72h
Time after treatment
pACC/ACC expression
relative to Non-treated cells
B
ACC
pACC
AMPK
pAMPK
β-actin
280 kDa
280 kDa
62 kDa
62 kDa
45 kDa

Figure S1

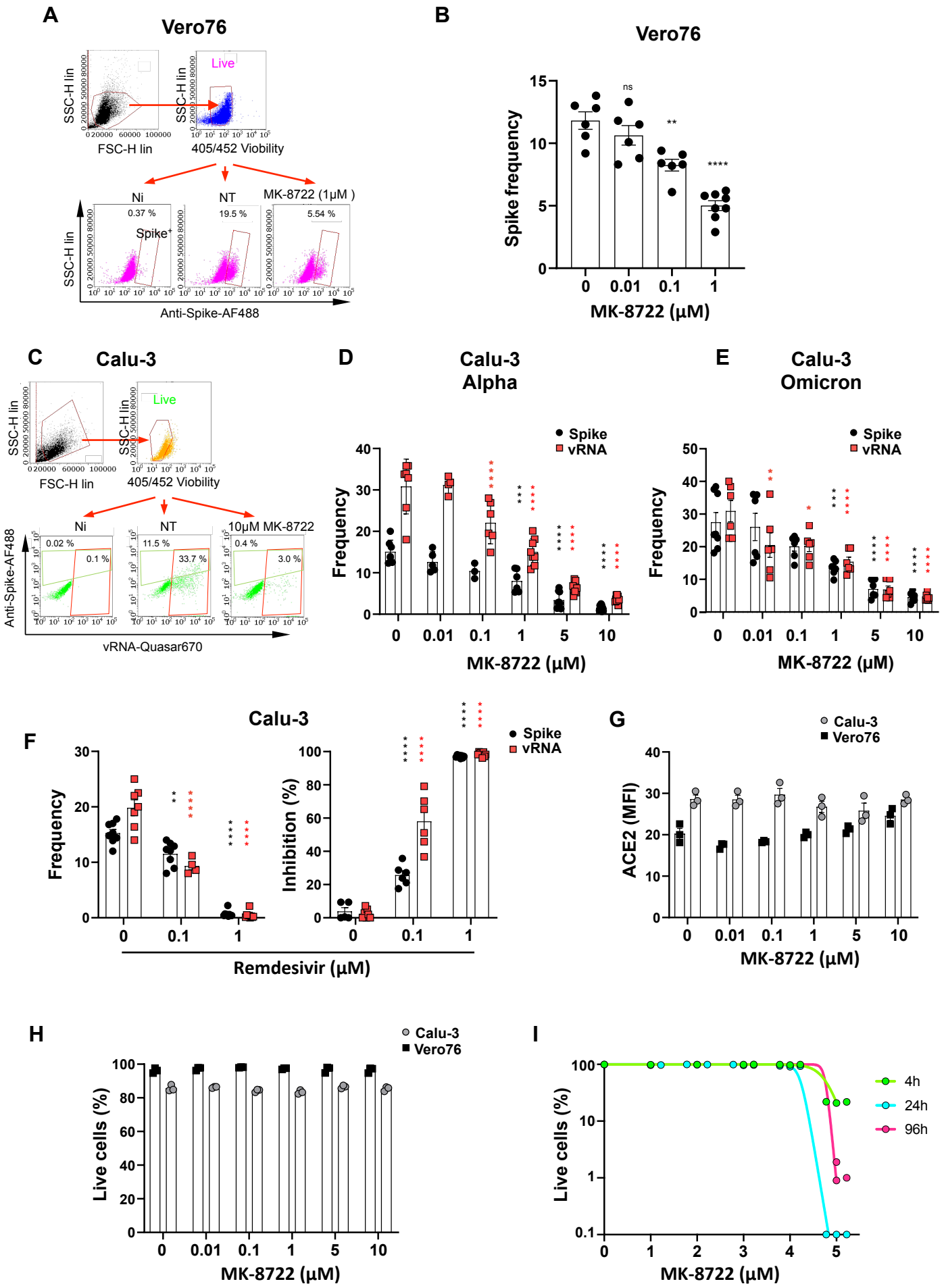
A
Vero76
SSC-H lin
FSC-H lin
Live
405/452 Viobility
Ni
NT
MK-8722 (1μM)
0.37 %
19.5 %
5.54 %
Spike+
Anti-Spike-AF488
B
Vero76
Spike frequency
ns
**
****
MK-8722 (μM)
C
Calu-3
10μM MK-8722
0.02 %
0.1 %
11.5 %
33.7 %
0.4 %
3.0 %
vRNA-Quasar670
D
Calu-3
Alpha
Spike
vRNA
Frequency
MK-8722 (μM)
E
Calu-3
Omicron
F
Inhibition (%)
Remdesivir (μM)
G
Calu-3
Vero76
ACE2 (MFI)
H
Live cells (%)
I
4h
24h
96h

Figure S2

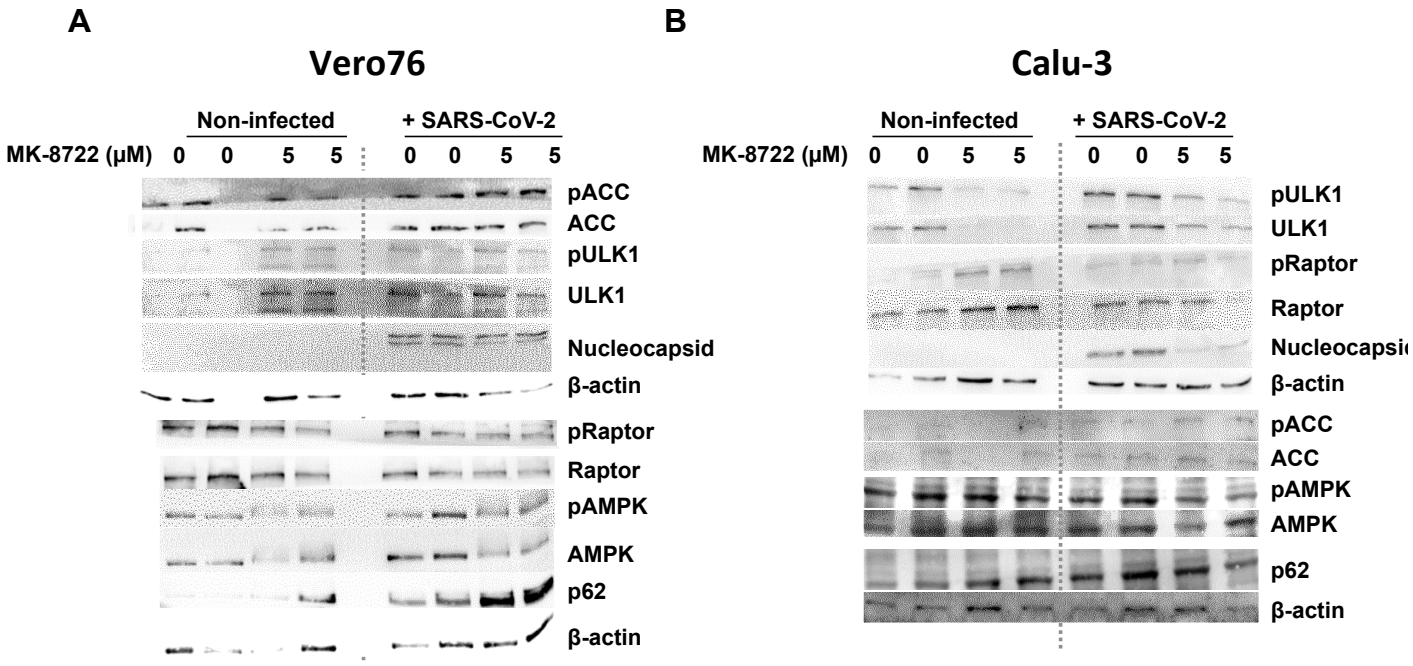
A
Vero76
Non-infected
+ SARS-CoV-2
MK-8722 (μM) 0 0 5 5 0 0 5 5
pACC
ACC
pULK1
ULK1
Nucleocapsid
β-actin
pRaptor
Raptor
pAMPK
AMPK
p62
β-actin
B
Calu-3
Non-infected
+ SARS-CoV-2
MK-8722 (μM) 0 0 5 5 0 0 5 5
pULK1
ULK1
pRaptor
Raptor
Nucleocapsid
β-actin
pACC
ACC
pAMPK
AMPK
p62
β-actin

Figure S3

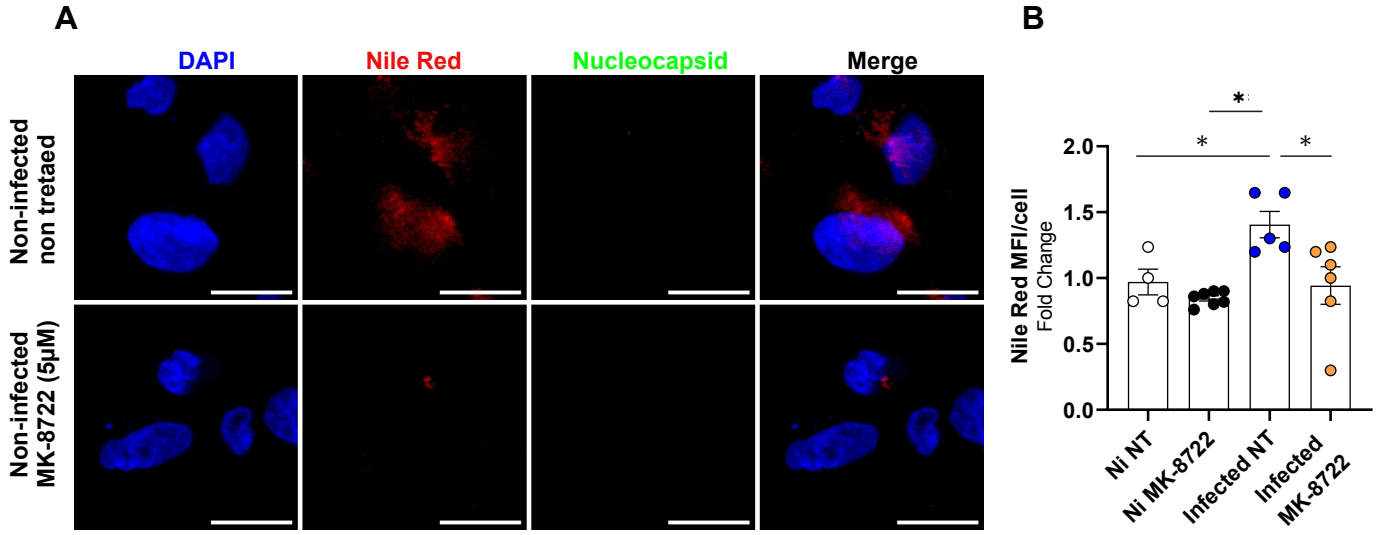
A
DAPI
Nile Red
Nucleocapsid
Merge
Non-infected non tretaed
Non-infected MK-8722 (5μM)
B
Nile Red MFI/cell
Fold Change
2.0
1.5
1.0
0.5
0.0
*
*
*
Ni NT
Ni MK-8722
Infected NT
Infected MK-8722

Figure S4

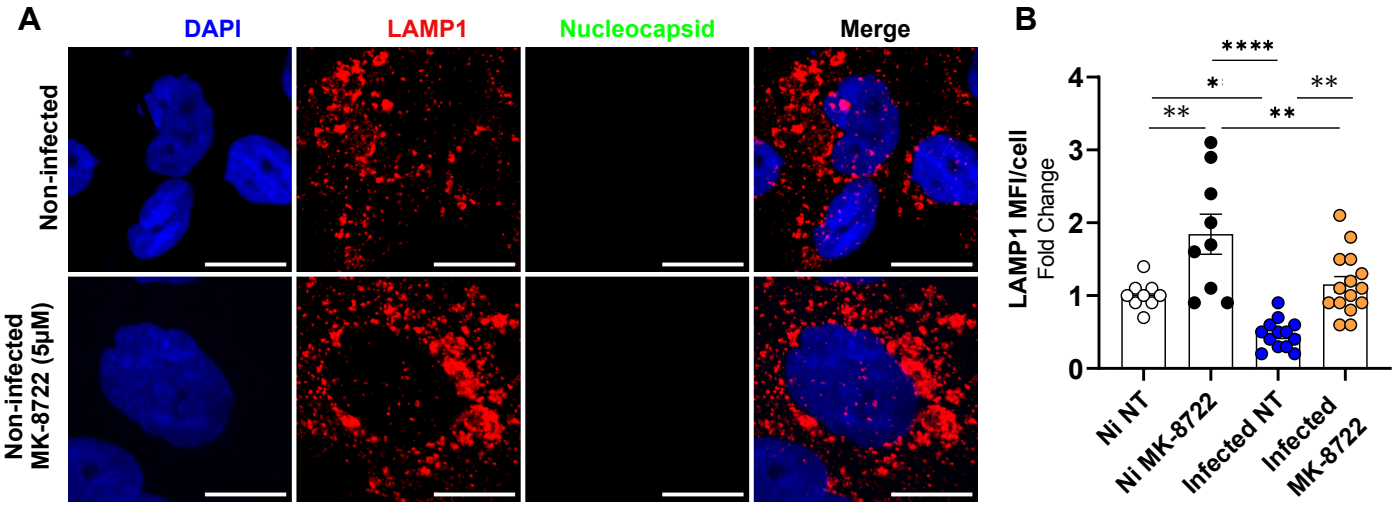
A
DAPI
LAMP1
Nucleocapsid
Merge
Non-infected
Non-infected
MK-8722 (5μM)
B
LAMP1 MFI/cell
Fold Change
0
1
2
3
4
****
*
**
**
**
Ni NT
Ni MK-8722
Infected NT
Infected
MK-8722

Figure S5

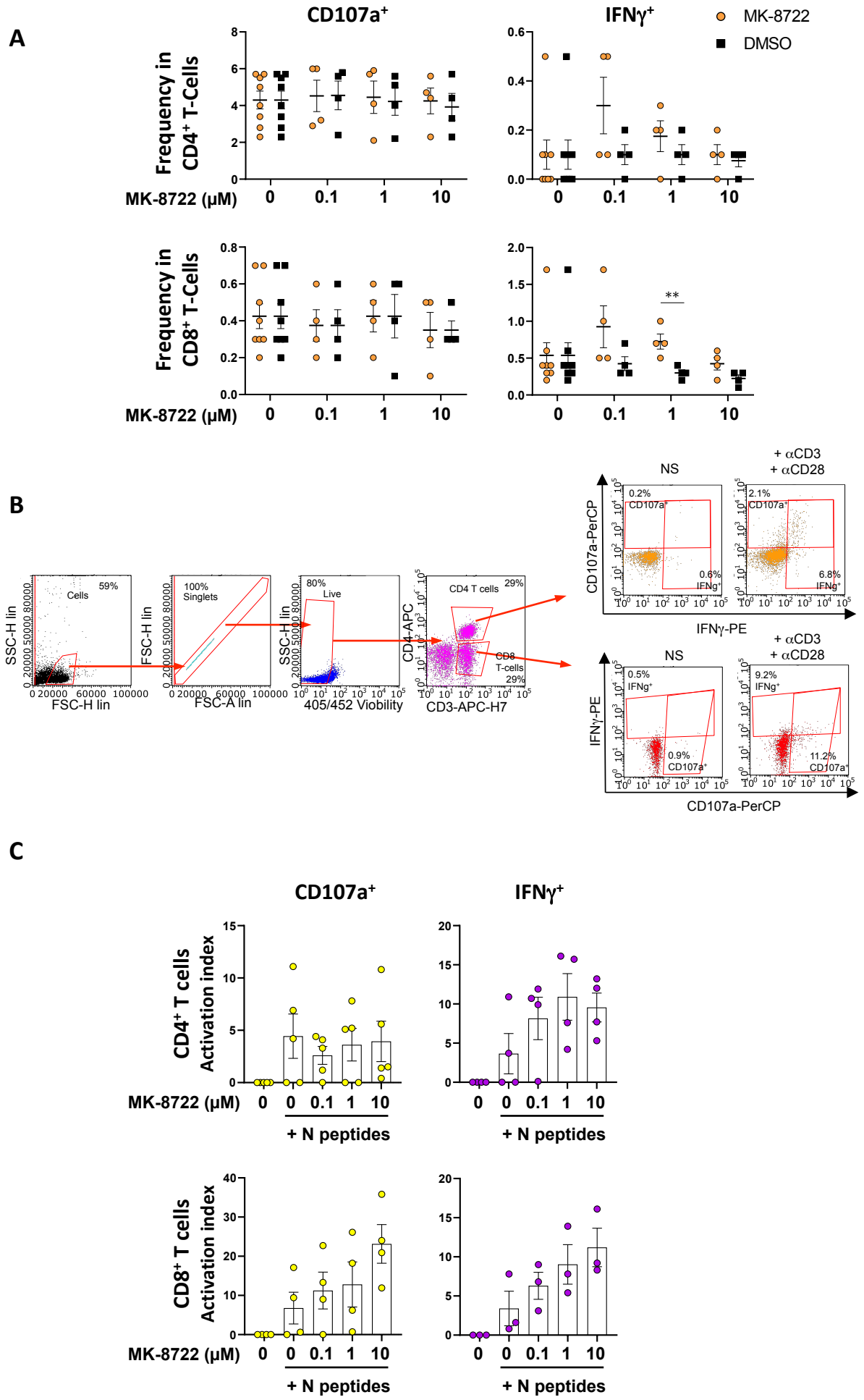
A
CD107a+
IFNγ+
MK-8722
DMSO
Frequency in CD4+ T-Cells
Frequency in CD8+ T-Cells
MK-8722 (μM)
0
0.1
1
10
**
B
SSC-H lin
FSC-H lin
Cells
59%
100% Singlets
FSC-A lin
80% Live
405/452 Viability
CD4-APC
CD3-APC-H7
CD4 T cells
29%
CD8 T-cells
29%
NS
+ αCD3 + αCD28
CD107a-PerCP
IFNγ-PE
0.2% CD107a+
0.6% IFNg+
2.1% CD107a+
6.8% IFNg+
0.5% IFNg+
0.9% CD107a+
9.2% IFNg+
11.2% CD107a+
C
CD107a+
IFNγ+
CD4+ T cells Activation index
CD8+ T cells Activation index
MK-8722 (μM)
+ N peptides

Figure S6

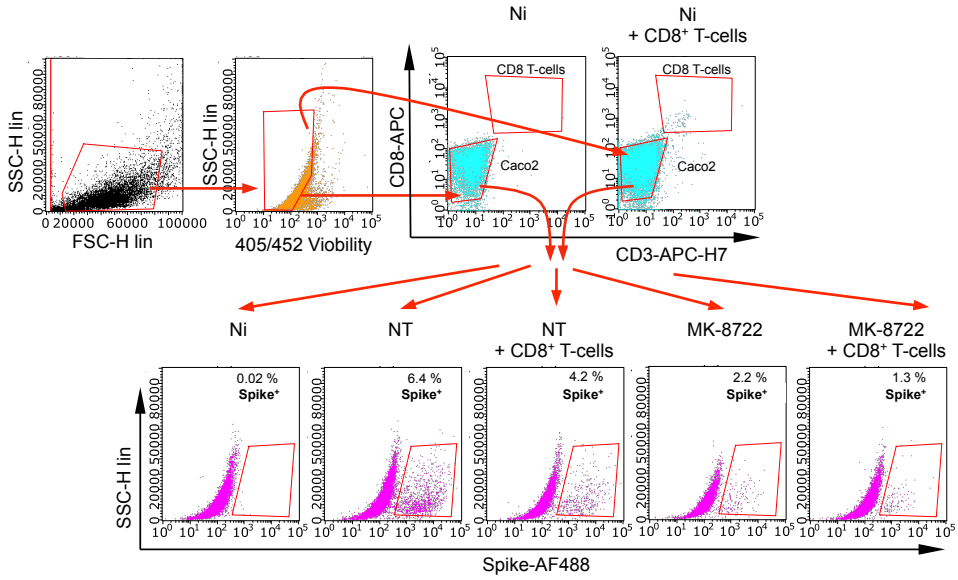
Ni
Ni
+ CD8+ T-cells
SSC-H lin
FSC-H lin
405/452 Viobility
CD8-APC
CD8 T-cells
Caco2
CD3-APC-H7
Ni
NT
NT
+ CD8+ T-cells
MK-8722
MK-8722
+ CD8+ T-cells
0.02 %
Spike+
6.4 %
Spike+
4.2 %
Spike+
2.2 %
Spike+
1.3 %
Spike+
Spike-AF488

Figure S7